JGR Solid Earth

RESEARCH ARTICLE
10.1029/2021JB021936

The Effect of Fe-Al Substitution on the Crystal Structure of $MgSiO_3$ Bridgmanite

Rong Huang[1,2], Tiziana Boffa Ballaran[1], Catherine A. McCammon[1], Nobuyoshi Miyajima[1], and Daniel J. Frost[1]

[1]Bayerisches Geoinstitut, Universität Bayreuth, Bayreuth, Germany, [2]Now at Department of Earth Sciences, University College London, London, UK

Key Points:

- The molar volumes of bridgmanite endmember components were determined to be $Fe^{3+}Fe^{3+}O_3$ > $MgFe^{3+}O_{2.5}$ > $Fe^{3+}AlO_3$ > $MgAlO_{2.5}$ > $AlAlO_3$ > $Fe^{2+}SiO_3$ > $MgSiO_3$
- Fe^{3+} and Al mainly occupy the A and B sites, respectively, at 25 GPa when Fe^{3+} = Al but disordering may be favored at higher pressures
- Pressure favors charge-coupled substitution over oxygen vacancy formation and may suppress Fe metal precipitation

Supporting Information:

Supporting Information may be found in the online version of this article.

Correspondence to:

R. Huang,
rong.huang@ucl.ac.uk

Citation:

Huang, R., Boffa Ballaran, T., McCammon, C. A., Miyajima, N., & Frost, D. J. (2021). The effect of Fe-Al substitution on the crystal structure of $MgSiO_3$ bridgmanite. *Journal of Geophysical Research: Solid Earth*, *126*, e2021JB021936. https://doi.org/10.1029/2021JB021936

Received 9 MAR 2021
Accepted 29 JUL 2021

Abstract The crystal chemistry of ten well-characterized bridgmanite single-crystals with Fe and Al contents ranging from 0 to 0.40 atoms per two-cation formula units were investigated by single-crystal X-ray diffraction. Structural refinements indicate that Fe^{3+} and Al mainly occupy the Mg and Si sites, respectively, when present in similar proportions. Molar volumes of bridgmanite endmember components were refined using data from this and previous studies and found to decrease in the order $Fe^{3+}Fe^{3+}O_3$ > $MgFe^{3+}O_{2.5}$ > $Fe^{3+}AlO_3$ > $MgAlO_{2.5}$ > $AlAlO_3$ > $Fe^{2+}SiO_3$ > $MgSiO_3$. $Fe^{3+}AlO_3$ charge-coupled substitution leads to an anisotropic increase of B-O bond distances, resulting in more distorted octahedral B sites and in a more significant increase of the *c*-axis with respect to the *a*- and *b*-axes. Valence bond calculations indicate that the A site is more compressible than the B site for all bridgmanite samples studied, implying that octahedral tilting and distortion will dominate the bridgmanite compression mechanism. Guided by these crystal chemical observations, bulk moduli of bridgmanite endmember components were estimated using results of previous studies. The volume changes of equilibria controlling the speciation of bridgmanite components were then calculated at conditions relevant to the top of Earth's lower mantle. The proportion of oxygen vacancy components is predicted to decrease with pressure. While the stability of the bridgmanite $Fe^{3+}AlO_3$ component will drive charge disproportionation to produce iron metal at the top of the lower mantle, this appears to be much less favorable by 50 GPa. An increase in the proportion of the $Fe^{3+}Fe^{3+}O_3$ bridgmanite component, however, may favor the formation of iron metal at higher pressures.

Plain Language Summary Fe-Al-bearing $MgSiO_3$ bridgmanite is the most abundant mineral in the Earth's lower mantle. Its physical and chemical properties, which are closely related to its crystal structure, play a major role in controlling processes in the Earth's lower mantle. In this study, we synthesized several bridgmanite single crystals with various compositions, which allowed the substitution mechanisms and site occupancies of Fe and Al in the structure to be determined. The changes in volume and structure resulting from the different substitution mechanisms were identified and can be used to explain the compressibility of different bridgmanite endmembers. The effect of pressure on the composition of bridgmanite was then predicted. We found that pressure should favor charge-coupled substitution where 3+ cations enter both the Mg and Si cation sites. The alternative mechanism, where 3+ cations enter the Si site and oxygen vacancies are created, is not favored with pressure. Also Fe^{3+} and Al may become disordered onto both the Mg and Si sites as pressure increases. The formation of Fe metal through reduction and oxidation of Fe^{2+} may be suppressed at greater depths in the lower mantle, therefore, the deep lower mantle may be less reduced than the shallower region.

1. Introduction

Iron- and aluminum-bearing $MgSiO_3$ bridgmanite, Brg, is most likely the predominant mineral of the Earth's lower mantle; hence its physical and chemical properties should account primarily for the seismic and transport properties of this region. Lower-mantle Brg is expected to accommodate a substantial amount of Fe and Al, which may vary between 0 and 0.40 atoms per formula unit (pfu) depending on the bulk rock composition (Hirose et al., 1999; Irifune & Ringwood, 1987; Irifune et al., 2010). At depths greater than 660 km, garnet, which is the main host for Al in the upper mantle and transition zone, transforms into Brg over a wide pressure interval, causing the Al_2O_3 content in pyrolitic Brg to increase from ~1 to 4–5 wt.% over the first 50 km of the lower mantle (Frost, 2008; Irifune, 1994; Wood, 2000) and in subducted basaltic crust

to be as high as ~16 wt.% (Hirose et al., 1999). The substitution of trivalent cations into the ABO_3 structure, as well as the presence of iron in two different valence states (Fe^{2+} and Fe^{3+}), causes the crystal chemistry of lower mantle Fe and Al-bearing Brg to be relatively complex. While Fe^{2+} substitutes for Mg^{2+} on the A site of Brg (Andrault et al., 1998; Lauterbach et al., 2000; McCammon et al., 1992), at least two competing mechanisms exist for the incorporation of trivalent cations M^{3+} ($M^{3+} = Fe^{3+}$, Al^{3+}) into the structure: (a) a charge-coupled (CC) substitution where the two trivalent cations substitute for Mg at the A site and Si at the B site simultaneously, that is, $Mg_A^{2+} + Si_B^{4+} = M_A^{3+} + M_B^{3+}$, creating compositions along the $MgSiO_3$-$M_2^{3+}O_3$ join (Frost & Langenhorst, 2002; Kojitani et al., 2007; Lauterbach et al., 2000; Vanpeteghem et al., 2006; Walter et al., 2004) and (b) an oxygen vacancy (OV) substitution where trivalent cations substitute for Si^{4+} at the B site and charge balance is achieved by the creation of oxygen vacancies, that is, $Si_B^{4+} + 0.5O_O^{2-} = M_B^{3+} + 0.5V_O^0$, which creates compositions along the $MgSiO_3$-$MgM^{3+}O_{2.5}$ join (Frost & Langenhorst, 2002; Kojitani et al., 2007; Lauterbach et al., 2000; Walter et al., 2006). The former CC mechanism results in the affinity of Al-bearing Brg for Fe^{3+}, which may have a strong influence on the redox state of the lower mantle (Frost et al., 2004; Lauterbach et al., 2000; McCammon, 1997). The latter OV mechanism is responsible for the formation of defect perovskites such as those found along the $CaTiO_3$ pervoskite-$CaFeO_{2.5}$ brownmillerite join (Becerro et al., 1999) where the oxygen vacancies formed likely have a strong influence on transport properties (Navrotsky et al., 2003).

Despite the potentially important effects of Fe^{3+} and Al substitution in Brg on lower mantle phase equilibria and redox state (Frost & Langenhorst, 2002; Irifune et al., 2010; Nakajima et al., 2012; Wood & Rubie, 1996) in addition to elasticity (Boffa Ballaran et al., 2012; Glazyrin et al., 2014; Kurnosov et al., 2017; Mao et al., 2017), rheological, and transport properties (Holzapfel et al., 2005; Ohta et al., 2008; Xu et al., 1998), the mechanisms by which Fe^{3+} and Al are accommodated into the Brg structure under differing conditions and compositions and how the different mechanisms affect the crystal chemistry of Brg are still not well constrained. This makes it difficult to evaluate the results of high-pressure studies particularly in terms of their applicability to the lower mantle. A determination of the partial molar volumes of Brg components, for example, is essential not only for constraining their effect on Brg density but also for a thermodynamic analysis of how the proportions of different Brg trivalent components will change with bulk composition or pressure in the lower mantle as a result of changes in partitioning or oxygen fugacity (fo_2). Due to the existence of several substitution mechanisms and the necessity to accurately determine both volumes and compositions (including $Fe^{3+}/\sum Fe$ ratio), very few data can currently be used for this purpose. The influence of trivalent cations on the crystal structure of Brg is also important for providing a mechanistic understanding of their effects on elastic and transport properties.

The $MgSiO_3$ Brg structure, space group *Pbnm* (Horiuchi et al., 1987; Ito & Matsui, 1978; Yagi et al., 1978) consists of a three-dimensional framework of corner-linked SiO_6 octahedra (B site) forming cavities occupied by Mg in bi-capped prism coordination (A site) described by eight oxygens with Mg-O distances smaller than 2.5 Å and 4 Mg-O distances larger than 2.7 Å (Figure 1a). This structure derives from an ideal cubic structure, with space group $Pm\bar{3}m$, through the tilting and distortion of the octahedral framework (e.g., Glazer, 1972; Howard & Stokes, 1998, 2005; Thomas, 1989). Several studies have experimentally examined the effect of Al and/or Fe^{3+} substitution on the unit-cell volume and equation of state (EoS) of Brg (Andrault et al., 2007; Boffa Ballaran et al., 2012; Catalli et al., 2010, 2011; Lundin et al., 2008; Nishio-Hamane et al., 2008; Ono et al., 2004; Saikia et al., 2009; Tange et al., 2009; Walter et al., 2004, 2006); however, very few studies have examined the structural variations in Brg associated with different cation substitutions, and the characterization of samples in the existing studies rarely extends to measurements of $Fe^{3+}/\sum Fe$ ratios. Several studies have suggested that Fe^{2+} substitutes mainly for Mg on the A site (Jephcoat et al., 1999; Kudoh et al., 1990; Parise et al., 1990; Sinmyo et al., 2011) while it has also been proposed that Fe^{3+} can substitute onto the Brg B site (Catalli et al., 2010; Hummer & Fei, 2012) and in Fe free Brg Al clearly also substitutes onto the A site (Grüninger et al., 2019; Liu, Akaogi, & Katsura, 2019; Liu, Ballaran, et al., 2019; Liu et al., 2017; Stebbins et al., 2003). However, no structural parameters have been reported that might allow the consequences of these substitutions to be examined. Vanpeteghem et al. (2006) studied the crystal chemistry of Fe^{3+} and Al-bearing Brg by means of single-crystal X-ray diffraction (XRD) and proposed that all Fe occupies the A site and that with increasing Fe^{3+} and Al content, the molar volume, the average A-O and B-O bond distances, and the BO_6 octahedra tilting all increase. This is in good agreement with the subsequent study of Glazyrin et al. (2014) on an Fe^{3+} and Al-rich Brg. However, the presence of impurities

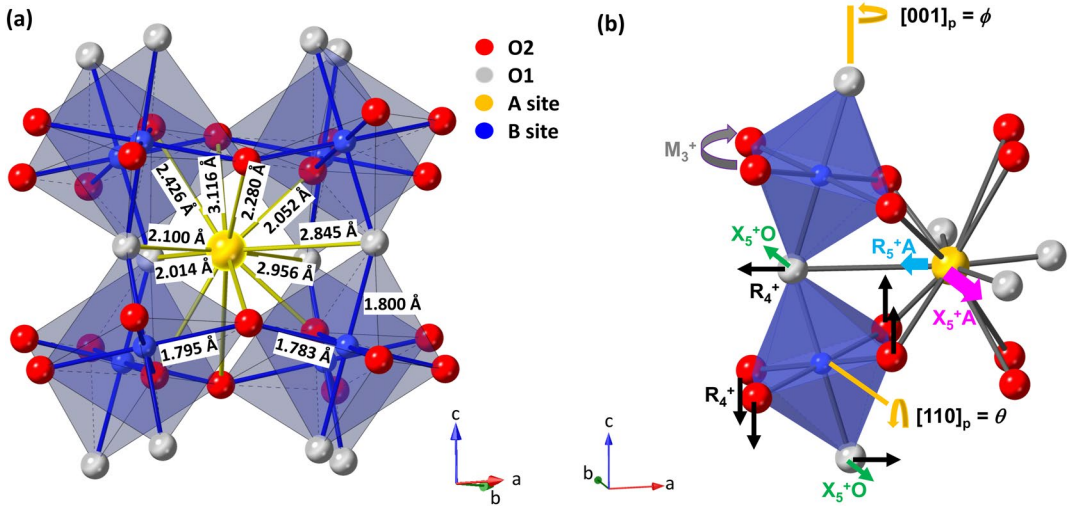

Figure 1. Structural model of $MgSiO_3$ Brg consisting of two cation sites. The A site is occupied by Mg (yellow) and the octahedral B site is occupied by Si (blue). (a) Individual A-O and B-O bond distances are indicated. (b) The orthorhombic distortion from the cubic aristotype perovskite structure is due to the in-phase (ϕ) and out-of-phase (θ) tilting of the octahedral framework. The atomic displacements associated with the orthorhombic distortion are also shown.

as well as the lack of knowledge on the $Fe^{3+}/\sum Fe$ ratio for the samples covered in these studies do not allow the contrasting effects of the different cation substitutions to be constrained.

In this study, single-crystal X-ray diffraction measurements were performed on ten well-characterized single-crystals of Brg with varying Fe^{3+} and Al contents from 0 to 0.40 atoms pfu, principally to determine the partial molar volumes of the Brg components. Some Brg samples were synthesized in assemblages with coexisting ferropericlase (Fp) to obtain the same silica activity as expected in a peridotitic lower mantle and to ensure a suitable environment to assess the importance of the OV substitution mechanism (Litasov et al., 2003; Navrotsky, 1999). The different substitution mechanisms were then carefully characterized in the recovered samples using a combination of electron microprobe, Mössbauer spectroscopy, and electron energy-loss spectroscopy measurements. The results of the single-crystal X-ray structural refinements provide insights into how the different cation substitution mechanisms affect the distortion of the Brg structure and as a consequence its elastic behavior. Moreover, based on the determined molar volumes of different Brg endmember components and previously reported elastic data, the stabilities of different Brg components with increasing pressure are estimated.

2. Experiments

2.1. Sample Syntheses

Glasses with the following nominal compositions: $Mg_{0.95}Fe_{0.05}Si_{0.95}Al_{0.05}O_3$ (En95), $Mg_{0.93}Fe_{0.07}Si_{0.93}Al_{0.07}O_3$ (En93), $Mg_{0.88}Fe_{0.12}Si_{0.88}Al_{0.12}O_3$ (En88, enriched with 95% ^{57}Fe), and $Mg_{0.83}Fe_{0.10}Si_{0.82}Al_{0.25}O_3$ (En83, enriched with 20% ^{57}Fe), were synthesized by melting dried reagent grade oxide mixtures of MgO, Al_2O_3, SiO_2, and Fe_2O_3 at 1650°C for 15 min in a 1 atm furnace followed by rapid quenching of the platinum crucible in water. The crushed glass powders were then ground under ethanol, cold pressed into pellets and then fired in a CO_2-CO gas-mixing furnace at 1250°C and at an fo_2 1 log unit above the iron-wüstite buffer (IW) for 48 h. To ensure that all Fe^{3+} was reduced in the rapidly quenched pellets, the samples were re-ground and re-fired at identical conditions for another 48 h. The recovered samples consisted of pyroxene containing only Fe^{2+}, as confirmed by means of Mössbauer spectroscopy. Glass En83 was not reduced and thus contained both Fe^{2+} and Fe^{3+} as a result of the glass making process in air. In order to study the influence of Fe and Al substitution on the crystal chemistry of Brg, large high-quality single-crystals with various compositions are needed. To achieve this, several strategies were followed (see Table S1 for details). In most experiments, pyroxene (En95, En93, and En88) or glass (En83) starting powders were mixed together with 5–10

wt.% $(Mg_{0.9}Fe_{0.1})O$, which was similarly synthesized and reduced so as to contain minimal Fe^{3+} (Table S1). In some Brg synthesis experiments, Fe metal (6–9 μm size powder) or hematite was also added to achieve relatively low or high fo_2 (Table S1). Water was added to all samples either using a syringe or as hydroxides ($Mg[OH]_2$ or $Al[OH]_3$) in order to promote the growth of large single-crystals. For one synthesis experiment (S6631), the starting material consisted of a ground mixture of MgO, $Mg(OH)_2$, $Al(OH)_3$, SiO_2, and Fe_2O_3 designed to produce a $(Mg_{0.8}Fe_{0.2})(Si_{0.8}Al_{0.2})O_3$ + 10 wt.% H_2O bulk composition.

The final starting compositions (Table S1) were loaded into gold foil capsules of 1.8 mm length and 0.8 mm diameter that were then placed inside platinum tubes 2 mm long and 1.0 mm in diameter, which were welded close at each end. The synthesis experiments were performed using 7 mm edge length Cr_2O_3-doped MgO octahedra and tungsten carbide cubes with truncations of 3 mm edge length that were compressed using a multi-anvil apparatus with a maximum compressive force equivalent to 1,200 tonnes. A $LaCrO_3$ tube heater was employed and temperature was estimated from the electrical power. The samples were first pressurized up to ~25 GPa, and then heated at 1300°C–1700°C for 2–12 h (Table S1). Textures indicate that this method results in smaller thermal gradient than when thermocouples are placed into each experiment. The runs were then quenched by turning off the electric power, and the pressure was released slowly over 20 h.

2.2. Sample Characterization

The recovered samples were mounted in epoxy resin and polished for microstructural observation and chemical analysis. Preliminary phase identification was performed using a micro-focused X-ray powder diffractometer (XRD; Bruker, D8 DISCOVER) equipped with a two-dimensional solid-state detector (VÅNTEC500) and micro-focus Co-$K\alpha$ radiation source (IμS) operated at 40 kV and 500 μA. A scanning electron microscope (SEM) (Zeiss Gemini 1530) equipped with a field emission gun and an energy-dispersive X-ray spectrometer (EDXS) was used to observe the sample textures and to characterize potential minor phases, which may be below the detection limit of XRD. Chemical compositions (Table 1) were analyzed with a JEOL JXA-8200 electron microprobe (EPMA), operating at 15 kV and 5 nA. The crystals of Brg were analyzed with a 3-μm defocused beam, to reduce beam damage, and all other solid phases were measured with a point beam. Counting times per element were 10 s on the peak and 5 s on the background. The following calibration standards were used: enstatite for Mg and Si, Fe metal for Fe, and corundum for Al. $MgSiO_3$ akimotoite single crystals, synthesized at 22 GPa and 1873 K, were used as a secondary standard for Mg and Si as akimotoite has a density close to that of Brg but is not beam sensitive. The analyses only proceeded once a Mg/Si ratio of one was obtained using the akimotoite standard. More than 20 points for each sample were measured in order to check the homogeneity of the Brg crystals.

The $Fe^{3+}/\sum Fe$ ratios in the Brg samples (Table 1) were determined using either Mössbauer spectroscopy or electron energy-loss spectroscopy (EELS). For two experiments, S6631, which contained Brg with ~0.26 Fe atoms pfu and H4615, whose starting material was enriched with 95% ^{57}Fe, we used single-crystals of Brg for the Mössbauer measurements. In particular, for S6631 only one very large (~250 × 250 × 50 μm^3) crystal was used; whereas for H4615 three single-crystals (~70 × 70 × 20 μm^3) were packed together to obtain a sufficient volume. Thick sections of multi-phase assemblages were used for other experiments with the thickness determined to produce an absorber thickness of ~5 mg Fe/cm^2 to avoid saturation effects. Mössbauer spectra were recorded in transmission mode for 20 to 48 h over sample regions of ~100–500 μm in diameter at room temperature using a constant acceleration Mössbauer spectrometer with a nominal 370 MBq ^{57}Co point source in a 12 μm Rh matrix. The velocity scale was calibrated relative to α-Fe. Spectra were fitted to pseudo-Voigt line shapes using the MossA program (Prescher et al., 2012), and the full transmission integral was used. The peaks of Fe in Brg were fitted by quadrupole doublets; the width and area of each quadrupole doublet component were constrained to be equal in the Mössbauer spectra collected for the polycrystalline samples, whereas the area ratio of doublet components was free to vary for samples S6631, H4615, and S6689, since quadrupole doublets of single crystals and samples with preferred crystal orientation may show area asymmetry (see Text S1, Figure S1 and Table S2 for details).

For two samples, S6732 and S6805, the $Fe^{3+}/\sum Fe$ ratio of Brg was determined using Fe-$L_{2,3}$ electron energy-loss near-edge structure (ELNES) spectroscopy because the synthesis runs contained larger proportions of Fp than in the other samples, which made separation of the individual contributions to Mössbauer spectra impossible. ELNES spectra were collected using an analytical transmission electron microscope

Table 1
Brg Averaged Compositions Measured by Electron Microprobe (EPMA) and Cation Proportions Normalized to Two Cations per Formula Unit

Sample	S6689	H4615	S6732	S6848	S6838	S7241	S6805	S6631
Chemical compositions of Brg by EPMA (wt.%)								
MgO	37.7(3)	34.2(3)	34.7(4)	33.3(4)	31.9(4)	33.9(3)	31.9(4)	28.3(3)
SiO_2	56.0(4)	51.7(3)	54.9(6)	54.0(4)	50.1(5)	48.8(4)	53.4(4)	44.4(3)
Al_2O_3	2.7(2)	5.7(2)	2.3(2)	3.3(2)	3.8(1)	9.3(3)	3.4(2)	9.2(2)
FeO	3.6(2)	8.1(4)	8.3(5)	10.1(5)	13.3(7)	7.8(4)	11.0(5)	17.2(6)
Total	100.0(4)	99.7(7)	100.2(7)	100.7(6)	99.1(6)	99.9(5)	99.7(7)	99.2(6)
$Fe^{3+}/\sum Fe$	0.85(5)[a]	0.83(8)[a]	0.30(9)[b]	0.47(8)[a]	0.81(5)[a]	0.95(2)[a]	0.28(5)[b]	0.87(5)[a]
Cation proportions normalized to a total of two cations								
A site								
Mg	0.950(5)	0.883 (5)	0.890 (8)	0.857 (8)	0.843 (7)	0.865 (6)	0.839 (7)	0.757 (7)
Fe^{2+}	0.008(3)	0.020 (9)	0.083(12)	0.077(12)	0.037(10)	0.006 (2)	0.116 (9)	0.034(13)
Fe_A^{3+}	0.043(6)	0.097(11)	0.027(14)	0.066(14)	0.119(12)	0.107 (6)	0.045(12)	0.209(15)
Al_A	–	–	–	–	–	0.023(10)	–	–
B site								
Si	0.945(5)	0.885(6)	0.944(8)	0.931 (6)	0.881 (9)	0.835(7)	0.930(7)	0.791 (6)
Al	0.055(5)	0.115(6)	0.047(4)	0.067 (5)	0.079 (2)	0.165(7)	0.070(7)	0.194 (4)
Fe_B^{3+}	–	–	0.009(9)	0.002 (8)	0.040(10)	–	–	0.015 (8)
O	2.994	2.991	2.986	2.998	3.000	2.982	2.987	3.000
Endmember components								
$MgSiO_3$	0.938	0.865	0.861	0.854	0.844	0.830	0.814	0.757
$Fe^{2+}SiO_3$	0.008	0.020	0.083	0.077	0.037	0.006	0.116	0.034
$M^{3+}M^{3+}O_3$	0.043	0.097	0.027	0.066	0.119	0.129	0.045	0.209
$MgM^{3+}O_{2.5}$	0.012	0.018	0.029	0.004	–	0.035	0.025	–

Note. The $Fe^{3+}/\sum Fe$ ratio has been determined using Mössbauer spectroscopy or electron energy-loss spectroscopy (EELS). $MgM^{3+}O_{2.5}$ = oxygen vacancy component; $M^{3+}M^{3+}O_3$ = charge-coupled substitution component. Sample S4253 (Boffa Ballaran et al., 2012) with the composition: $^{A}(Mg_{0.60}Fe^{2+}_{0.03}Fe^{3+}_{0.37})\ ^{B}(Si_{0.63}Al_{0.36}Fe^{3+}_{0.01})O_3$ has the following endmember components: $MgSiO_3 = 0.600$, $Fe^{2+}SiO_3 = 0.030$, $M^{3+}\ M^{3+}O_3 = 0.370$.
[a]Means of Mössbauer spectroscopy measurements. [b]Means of EELS measurements.

(ATEM, Philips CM20FEG) equipped with a parallel electron energy-loss spectrometer (PEELS Gatan 666), operating at 200 kV. TEM thin foils were prepared using either conventional Ar-milling or a focused ion beam (FIB) instrument. The TEM experiments were performed at −170°C using a liquid nitrogen-cooling holder. Fe-$L_{2,3}$ edge ELNES spectra were collected in diffraction modes at the thinnest part of the ion-thinned sample and a typical ELNES spectrum for Brg is shown in Figure S2. Quantification of the Fe-$L_{2,3}$ edge ELNES was performed following the procedure described by van Aken et al. (1998) and van Aken and Liebscher (2002), using an empirically calibrated universal curve. The EELSA program (https://github.com/CPrescher/EELSA) was used to evaluate the $Fe^{3+}/\sum Fe$ ratios reported in Table 1. The time-series analyses of the spectra showed that the measured ratios did not change significantly with increasing electron irradiation time up to 80 s of acquisition, which would otherwise indicate iron oxidation during the EELS measurement (Lauterbach et al., 2000).

2.3. Single-Crystal X-Ray Diffraction and Structural Refinements

Two further samples, H3004 and S4253, synthetized in a previous study (Boffa Ballaran et al., 2012) and having respectively a $MgSiO_3$ endmember composition and a very Fe and Al-rich composition

($Mg_{0.60}Fe^{2+}_{0.03}Fe^{3+}_{0.38}Si_{0.63}Al_{0.36}O_3$), have been used in this study together with those recovered from the syntheses performed in this study. Ten single-crystals of Brg with Fe and Al contents varying from 0 to 0.40 atoms pfu were selected based on their optical appearance, lack of twinning, and their narrow diffraction profiles. Unit-cell lattice parameters were determined using the eight-position centering method (Angel et al., 2000; King & Finger, 1979) on a HUBER four-circle diffractometer equipped with Mo $K\alpha$ radiation operating at 50 kV and 40 mA and a point detector operated using the *SINGLE* software (Angel & Finger, 2011). Intensity data were collected at ambient conditions using an Xcalibur diffractometer with Mo $K\alpha$ radiation ($\lambda = 0.71073$ Å) operated at 50 kV and 40 mA, equipped with a CCD detector and a graphite monochromator. Omega scans were chosen to obtain full coverage of the reciprocal sphere up to $2\theta_{max} = 80°$, with an exposure time of 20 s/frame and a step size of 0.5° at a crystal-detector distance of 45.1 mm.

Lorentz and polarization factors together with an analytical absorption correction based on the crystal shape were performed for the correction of the reflection intensities using the CrysAlis package (Oxford Diffraction, 2006). Symmetrically equivalent reflections were merged and structure refinements were performed based on F^2 using the SHELX97 program package (Sheldrick, 2008) in the WinGx System (Farrugia, 1999). The structure refinements were carried out in space group *Pbnm* starting with the atomic coordinates reported by Horiuchi et al. (1987). Neutral scattering factors for Mg, Si, Al, Fe, and oxygen were used (Allen et al., 1992), and all atoms were refined anisotropically. In order to model the cation distribution of Al and Fe between the A- and B- sites, we have taken the following steps: (a) the occupancies of Fe and Mg were refined at the A site with their sum constrained to be equal to 1; (b) since refinements using the scattering factors of Si and Fe at the B site always resulted in a negative occupancy of Fe, the B site has been refined using only the Si scattering factor with the occupancy of Si free to vary; (c) oxygen occupancies have been fixed to the value of 1, given that the amount of vacancies indicated by the EPMA analyses is well below the sensitivity of the structural refinements. Details of data collection and refinement parameters, fractional occupancies, atomic coordinates and anisotropic displacement parameters are provided in a Crystallographic Information File (CIF) in the supplementary information.

3. Results

3.1. Al and Fe Substitution Mechanisms in Bridgmanite

The assemblages recovered from the high-pressure syntheses are summarized in Table S1, and the average compositions of the Brg crystals are reported in Table 1. The Fe and Al contents of these well-characterized Brg samples extend up to 0.40 Fe and 0.36 Al atoms pfu, respectively. Based on cation radii, it would seem logical that Fe^{3+} partitions more favorably into the Brg A site and Al^{3+} into the B site (Shannon, 1976) as proposed previously (McCammon et al., 2013; Vanpeteghem et al., 2006). As the Mössbauer spectra (see Text S1, Figure S1 and Table S2) are inconclusive in determining the Fe^{3+} site assignment (Lin et al., 2013; McCammon, 1998), we follow the assumption that cations partition between the two sites in accordance with their radii. Several lines of evidence in the single-crystal diffraction results support this, as will be shown later. A simple procedure is followed, therefore, to estimate the site occupancies based on the EPMA analyses, whereby the B site is first filled with the Al cations and the A site with Fe^{3+}. If Si + Al are larger than 1, extra Al is placed on the A site and conversely, if Mg + Fe^{2+} + Fe^{3+} are larger than 1, extra Fe^{3+} is placed on the B site. The resulting cation distribution between the A and B sites and the proportions of Brg components are reported in Table 1. For most of the samples, this procedure indicates insignificant amounts of Fe^{3+} entering the B site, but sample S6838 is determined to have ~0.04(1) atoms pfu of Fe^{3+} at the B site (Table 1). This occurs because the amount of Fe^{3+} cations exceeds those of Al.

The mean atomic numbers (m.a.n.) of cations at the A- and B-sites determined by means of the single-crystal structural refinements are in good agreement with the cation assignments resulting from EPMA analyses (Table S3), providing some confirmation for the preference of Fe^{3+} and Al for the A and B sites, respectively, when both are present. The small differences between the two estimates are likely due to the combined uncertainties of the structural refinement and chemical analyses. The existence of at least some amount of trivalent cation disorder between the two sites cannot be excluded, although as discussed later, if this were significant it would show up in the molar volumes and octahedral bond distances.

Table 2
Unit-Cell Lattice Parameters of the Brg Single-Crystals Investigated in This Study

Sample	a (Å)	b (Å)	c (Å)	V (Å^3)	V_m (cm^3/mol)
H3004	4.7767(5)	4.9294(5)	6.8964(5)	162.38(3)	24.447(4)
S6689	4.7821(10)	4.9401(10)	6.9152(10)	163.37 (5)	24.595(8)
H4615	4.7881 (1)	4.9528(2)	6.9376(1)	164.52 (1)	24.769(1)
S6732	4.7907(5)	4.9392(6)	6.9170(6)	163.67(3)	24.641(4)
S6848	4.7938(3)	4.9452(3)	6.9257(3)	164.18(2)	24.718(2)
S6838	4.7982(4)	4.9624(4)	6.9517(4)	165.52(2)	24.920(3)
S7241	4.7883(9)	4.9607(9)	6.9563(9)	165.23(5)	24.876(7)
S6805	4.7969(5)	4.9452(5)	6.9267(5)	164.32(2)	24.738(4)
S6631	4.8003(2)	4.9742(2)	6.9714(2)	166.46(1)	25.061(2)
S4253	4.8107(4)	4.9996 (1)	7.0264(2)	169.00(1)	25.443(2)

The Brg compositions along with well-characterized samples from previous studies (Frost & Langenhorst, 2002; Lauterbach et al., 2000; Liu et al., 2020; Saikia et al., 2009) can be plotted in a ternary diagram with respect to the (Mg, Fe^{2+})O-SiO_2-(Al, Fe^{3+})$_2O_3$ components (Figure S3). Substitution trends expected along the CC $MgSiO_3$-$(M^{3+})_2O_3$ join (where M^{3+} = Fe^{3+} or Al^{3+}) and the OV $MgSiO_3$-$MgM^{3+}O_{2.5}$ joins are also indicated. Note that the OV component $MgM^{3+}O_{2.5}$ is essentially $MgAlO_{2.5}$ as samples displaying this component contain negligible B site Fe^{3+}. Similarly, the CC component, $M^{3+}M^{3+}O_3$, is mainly $Fe^{3+}AlO_3$. As expected, the samples are mainly dominated by the CC substitution (mainly $Fe^{3+}AlO_3$) in spite of the fact that some of them were synthesized in the presence of Fp, which has been shown to promote the OV mechanism in iron-free samples (Liu, Akaogi, & Katsura, 2019; Liu, Ballaran, et al., 2019; Navrotsky et al., 2003). Some samples deviate slightly from the trend but the OV component does not exceed 0.04 pfu for the investigated single-crystals. Three samples (S6732, S6848, and S6805) also contain a considerable amount of $Fe^{2+}SiO_3$ (7–12 mol.%) component, which enables us to examine the effect of Fe^{2+} on the Brg structure and S6838 contains 4 mol.% of the $Fe^{3+}Fe^{3+}O_3$ component, which provides some information on the effects of Fe^{3+} on the Brg B-site.

3.2. Molar Volumes of (Fe, Al)-Bearing $MgSiO_3$ Bridgmanite

The unit-cell lattice parameters and molar volumes of the Brg single-crystals investigated in this study are reported in Table 2. The molar volumes (V_m) of the investigated samples are plotted against the sum of their endmember components and compared with published data in Figure 2. The trend defining the $Fe^{2+}SiO_3$ substitution is well constrained by studies that used iron or graphite capsules to ensure minimal Fe^{3+} contents (Jephcoat et al., 1999; McCammon et al., 1992; Tange et al., 2009). The V_m of the $Fe^{2+}SiO_3$ endmember, assuming a linear relation between the endmember volumes, is 25.35(2) cm^3/mol, calculated using a linear fit through these data. The trend defining the variation of the Brg V_m along the $MgSiO_3$-$Fe^{3+}AlO_3$ join has been constrained using only volumes reported for samples for which $Fe^{3+}/\sum Fe$ ratios were measured and for which the $Fe^{2+}SiO_3$ and OV components were minimal. The volumes were linearly corrected for the contribution of the $Fe^{2+}SiO_3$ component (i.e., $V_m = X_{MgSiO_3} \times V_{MgSiO_3} + X_{Fe^{2+}SiO_3} \times V_{Fe^{2+}SiO_3} + X_{Fe^{3+}AlO_3} \times V_{Fe^{3+}AlO_3}$). The resulting molar volume for the $Fe^{3+}AlO_3$ endmember is 27.09(6) cm^3/mol. Most samples investigated in this study lie between the two linear trends of the $Fe^{3+}AlO_3$ and $Fe^{2+}SiO_3$ substitution mechanisms (Figure 2a). The V_m of the remaining Brg samples (Table 2) were then expressed in terms of the summation of molar volumes of the four endmember components in order to constrain $V_{MgM^{3+}O_{2.5}}$. This resulted in the value 26.70(18) cm^3/mol, which is statistically identical to the value of $V_{MgAlO_{2.5}}$ of 26.64(10) cm^3/mol reported by Liu, Akaogi, and Katsura (2019) from an examination of iron-free samples. This implies that the creation of OV has a similar effect on the structure of Brg independent of whether this substitution occurs in an Fe- and Al-bearing or just an Al-bearing system, which further supports the notion that in the Fe- and Al-bearing system very little Fe^{3+} enters the B site. Sample S6838 plots above the $Fe^{3+}AlO_3$ trend, which is consistent with it being the only sample where the Fe^{3+} content is significantly larger than Al, which then forces Fe^{3+} onto the B-site to provide charge balance through an $Fe^{3+}Fe^{3+}O_3$ component. Even a small component of B-site Fe^{3+} therefore leads to an obvious effect on V_m, which again supports the concept that very little Fe^{3+} enters the B-site unless Fe^{3+} > Al. From previous analyses reported for Al-free samples (Catalli et al., 2010; Hummer & Fei, 2012), it is possible to estimate the V_m of the $Fe^{3+}Fe^{3+}O_3$ endmember to be 29.55(3) cm^3/mol, which is the largest in the systems examined, explaining why the V_m of the investigated Brg is so sensitive to this endmember. For completeness, it is also possible to estimate a V_m of 27.65(1) cm^3/mol for the $MgFe^{3+}O_{2.5}$ endmember using analyses reported by Hummer and Fei (2012). The molar volumes for the different Brg endmembers, therefore, decrease in the order $Fe^{3+}Fe^{3+}O_3$ > $MgFe^{3+}O_{2.5}$ > $Fe^{3+}AlO_3$ > $MgAlO_{2.5}$ > $AlAlO_3$> $Fe^{2+}SiO_3$ > $MgSiO_3$ (Table 3). It should be noted that this analysis assumes a linear dependence of V_m on composition as there are no detectable deviations from ideal mixing over the accessible compositional range.

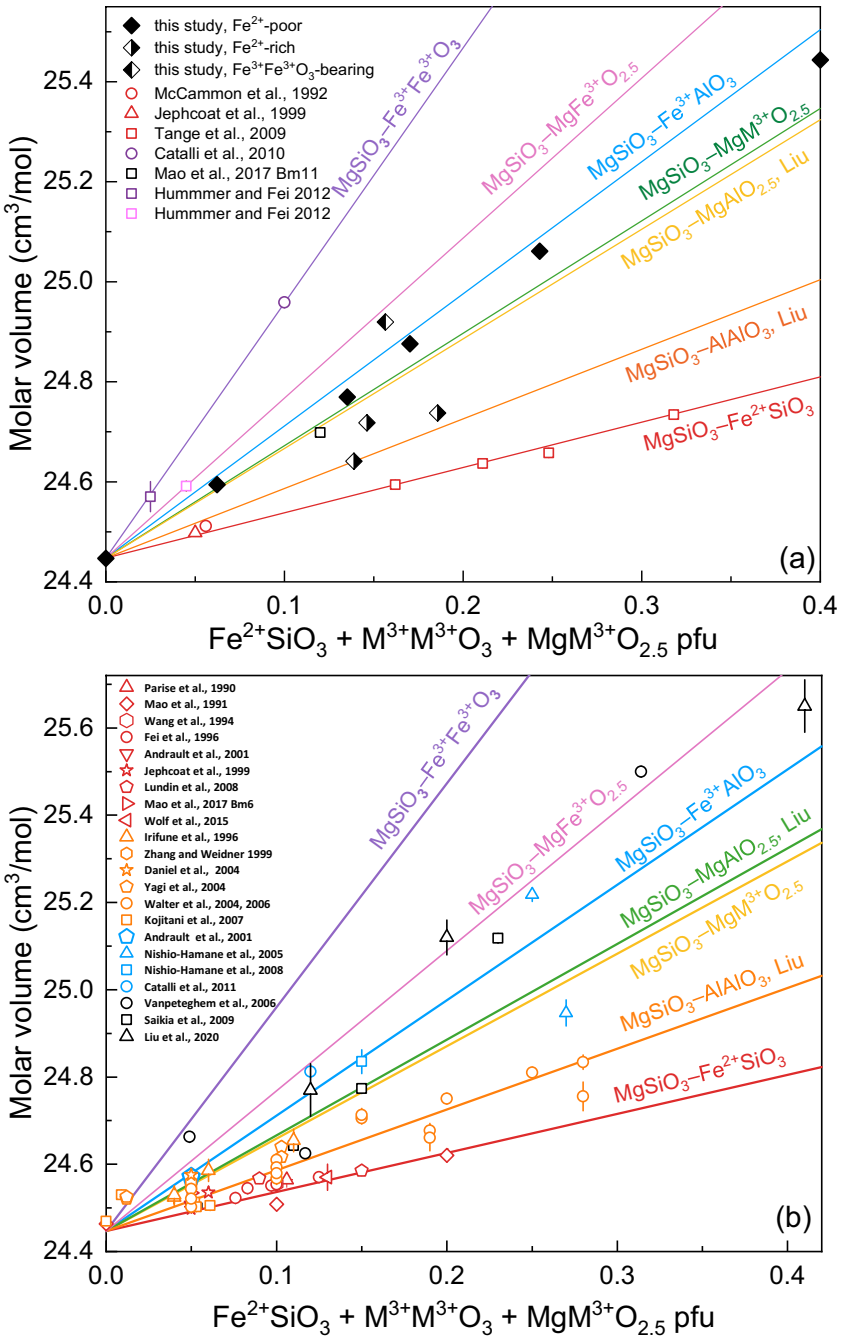

Figure 2. Variation of the molar volumes of Brg as a function of the sum of components other than $MgSiO_3$. The seven colored lines are the molar volume linear variations along the indicated joins. The Fe-free joins are taken from Liu, Akaogi, and Katsura (2019) and Liu et al. (2020). Data sets dominated by the substitution of a particular component are shown using the same color as that of the curve for the corresponding system. The black symbols are samples that exhibit a combination of several substitution mechanisms. (a) Results from the current study and previous studies employed for fitting the endmember volumes. Note that in determining the $Fe^{3+}AlO_3$ curve the data points employed have been corrected for their $Fe^{2+}SiO_3$ content. Left half-filled diamonds indicate sample S6838, which contains 0.04 pfu $Fe^{3+}Fe^{3+}O_3$; right half-filled diamonds indicate three Fe^{2+}-rich samples (S6805, S6732, and S6848) containing 0.07–0.12 pfu $Fe^{2+}SiO_3$ and solid diamonds represent other samples which have ≤ 0.03 pfu $Fe^{2+}SiO_3$. (b) Comparison with other studies whose data were not used for obtaining the endmember volumes. The uncertainties that are not shown are smaller than the symbols.

Table 3
Molar Volumes of Brg Endmember Components

Endmember components of Brg	Molar volume (cm^3/mol)
$MgSiO_3$	24.447(4)
$Fe^{2+}SiO_3$	25.35(2)
$Fe^{3+}AlO_3$	27.09(6)
$MgM^{3+}O_{2.5}$	26.70(18)
$MgAlO_{2.5}$ [a]	26.64(10)[a]
$AlAlO_3$ [b]	25.84(3)[b]
$Fe^{3+}Fe^{3+}O_3$	29.55(3)
$MgFe^{3+}O_{2.5}$	27.65(1)

Note. The standard deviations for the $Fe^{3+}Fe^{3+}O_3$ and $MgFe^{3+}O_{2.5}$ endmember volumes are small due to the limited number of data points available.
[a]From Liu, Akaogi, and Katsura (2019). [b]From Liu et al. (2020).

Results from previous studies, which have not been included in the fitting procedure to obtain the endmember molar volumes due to uncertainties in the compositions or the presence of other elements, are also plotted for comparison in Figure 2b. Studies on $(Mg,Fe^{2+})SiO_3$ Brg, which either reported nominal compositions (Andrault et al., 2001; Lundin et al., 2008; Mao et al., 1991; Parise et al., 1990) or reported small amounts of Fe^{3+} in the investigated samples (Mao et al., 2017 Bm6) give Brg molar volumes that lie very close to the $Fe^{2+}SiO_3$ trend (Figure 2b). Some of the diamond anvil cell (DAC) experiments reporting only $Fe^{3+}AlO_3$ substitution based on the starting compositions fall exactly on our $Fe^{3+}AlO_3$ trend (Andrault et al., 2001; Nishio-Hamane et al., 2008), while others deviate (Catalli et al., 2011; Nishio-Hamane et al., 2005). Where these volumes are larger than the $MgSiO_3$-$Fe^{3+}AlO_3$ join some Fe^{3+} may have entered the B site, most likely due to the proportion of Fe^{3+} being greater than Al. Where volumes are smaller than the trend this may be due to iron reduction to form some $Fe^{2+}SiO_3$ component or iron loss during laser heating. The large deviation of the $Fe^{3+}AlO_3$-rich samples reported by Vanpeteghem et al. (2006) is most likely due to the presence of additional Na and Ti in some of these samples (Figure 2b). The three data points from Liu et al. (2020) have larger molar volumes than our $Fe^{3+}AlO_3$ substitution trend, which may result from inaccuracy in the determination of the Brg volumes due to the use of a micro-focused XRD. The V_0 reported for a very Fe-rich Brg with the composition $(Mg_{0.46}Fe^{3+}_{0.53})(Si_{0.49}Fe^{3+}_{0.51})O_3$ (Liu et al., 2018) was 2% larger than predicted from our $Fe^{3+}Fe^{3+}O_3$ trend line, most likely because the room pressure volume in Liu et al. (2018) was determined by extrapolating back to room pressure using a second order Birch-Murnaghan EoS. Nonetheless, this result is consistent with the $Fe^{3+}Fe^{3+}O_3$ endmember having the largest V_m of the components considered.

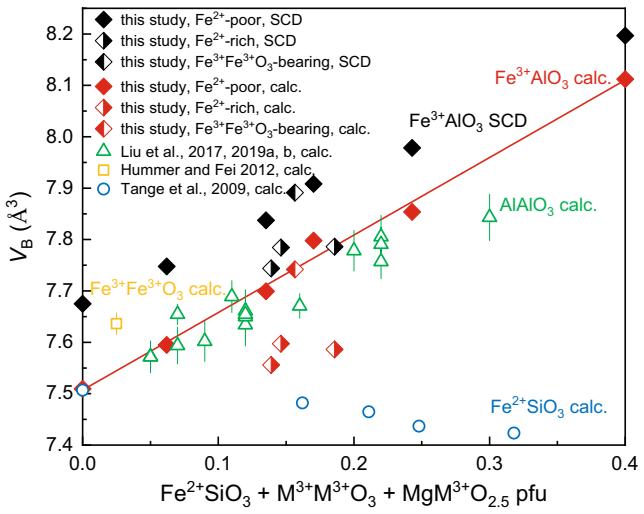

Figure 3. The polyhedral volumes of the B site in Brg as a function of the sum of endmember components other than $MgSiO_3$. The polyhedral volumes of $Fe^{3+}AlO_3$ CC-dominant Brg calculated from the lattice parameter as discussed in the text are shown by red diamonds and those obtained from single-crystal X-ray diffraction (SCD) are shown as black diamonds. Symbols are the same as in Figure 2a. The circles, triangles, and squares indicate the polyhedral volumes calculated from the lattice parameters for the $Fe^{2+}SiO_3$ (Tange et al., 2009); $AlAlO_3$ (Liu, Akaogi, & Katsura, 2019; Liu, Ballaran, et al., 2019; Liu et al., 2017) and $Fe^{3+}Fe^{3+}O_3$ (Hummer & Fei, 2012) samples, respectively. Errors are within the symbol size when not indicated.

We can try to rationalize the endmember V_m for the different substitutions in terms of the A and B site polyhedral volumes. For the samples from this study, the single-crystal diffraction refinements can be used to precisely determine these polyhedral volumes. However, as such structural data do not exist for other components, we have to estimate these volumes from the unit-cell lattice parameters. These calculations assume that the orthorhombic structure arises from the tilting of regular and undistorted octahedra, and as already reported (Mitchell, 2002; Sinmyo et al., 2014; Zhao et al., 1993a, 1993b), the values obtained underestimate the actual tilting and octahedral bond lengths due to distortions. However, if we compare the octahedral volumes, V_B, obtained from the structural refinements with that calculated from an average B-O bond distance obtained from the lattice parameters as <B-O> = b * c/(4 * a) (Mitchell, 2002), we observe near parallel trends with increasing $Fe^{3+}AlO_3$ substitution (Figure 3). Therefore, we can use the unit-cell lattice parameters reported in previous studies (Hummer & Fei, 2012; Liu, Akaogi, & Katsura, 2019; Liu, Ballaran, et al., 2019; Liu et al., 2017; Tange et al., 2009) in order to describe, at least as a first approximation, the variation of V_B as a function of different cation substitutions (Figure 3). V_B increases with $AlAlO_3$ substitution (green triangles) with almost the same slope as that observed for the $Fe^{3+}AlO_3$ substitution, as expected, given the substitution of the larger Al cation ($^{VI}r_{Al}$ = 0.675 Å, Shannon, 1976) for the smaller Si cation ($^{VI}r_{Si}$ = 0.540 Å) at the B site. The difference in molar volumes between the $Fe^{3+}AlO_3$ and $AlAlO_3$ components is therefore likely due to differences in the extent of octahedral tilting, given the different radii of Fe^{3+} and Al substituting at the A site. The $Fe^{3+}Fe^{3+}O_3$ substitution, which requires the larger Fe^{3+} cation ($^{VI}r_{Fe^{3+},HS}$ = 0.785 Å) to occupy the B site,

increases V_B to a much larger extent (yellow square) and is the primary reason for the very large molar volume of the $Fe^{3+}Fe^{3+}O_3$ component. As expected, the $Fe^{2+}SiO_3$ substitution (blue circles) has practically no effect on the octahedral volume, since Fe^{2+} substitutes only at the A site. The marginal decrease of V_B observed for the data reported by Tange et al. (2009) is very likely a secondary effect due to a decrease of the octahedral tilting in these Brgs. The slightly larger molar volume of the $Fe^{2+}SiO_3$ component with respect to the Brg endmember is therefore due simply to the larger A site.

3.3. Distortion of the Perovskite-Type Structure of Bridgmanite

The orthorhombic distortion of the Brg structure with respect to the ideal cubic $Pm\bar{3}m$ aristotype is due to the tilting of the octahedral units and can be described using tilt components around "pseudo-cubic" axes, that is, around the axes of the cubic aristotype structure (Glazer, 1972). The simplest method for calculating the tilt angles is to derive them from the unit-cell lattice parameters but as already mentioned this assumes that the octahedral framework is rigid and regular and tilting angles calculated in this way are usually underestimated (e.g., Mitchell, 2002; Sinmyo et al., 2014). More realistic tilt angles can be calculated using the atomic coordinates of the oxygen atoms (Kennedy et al., 1999; Zhao et al., 1993a, 1993b) whose displacements from the cubic atomic positions result not only from tilting but also from the distortion of the octahedral sites. A clear and unambiguous way to separate the effects of distortion and tilting of perovskite structures is provided by analysis of the irreducible representations (Irreps) describing the displacive modes of the A cation and oxygens from the atomic positions of the cubic aristotype structure (Howard & Stokes, 1998, 2002; Perez-Mato et al., 2010). The five mode displacements for the *Pbnm* space group associated with the points X (0, 0, 1/2), M (1/2, 1/2, 0), and R (1/2, 1/2, 1/2) of the Brillouin zone are the in-phase and out-of-phase tilt patterns, represented by the two Irreps M_3^+ and R_4^+, respectively; an octahedral basal distortion represented by the Irrep M_2^+, and the Irreps R_5^+ and X_5^+ each of which describe displacements of both the oxygen atoms and the A cations away from their positions in the cubic aristotype, which for the A cations is the center of an undistorted polyhedron (Figure 1; the notation is taken from Miller & Love, 1967). The program ISODISTORT (Campbell et al., 2006) has been used to decompose the Brg structures refined in this study into these five symmetry-adapted modes with respect to ideal parent cubic structures that have identical volumes to that of our samples (Table S4).

A sketch describing the R_4^+, M_3^+, X_5^+, and R_5^+ modes in the orthorhombic perovskite structure is shown in Figure 1b, while the displacement amplitudes of the same modes are shown in Figures 4a–4c as a function of OV + CC component concentration. Values of zero for these terms would correspond to an undistorted cubic perovskite. The amplitudes of M_2^+ and R_5^+ O are very small in Brg and are therefore ignored. The R_4^+ and M_3^+ modes corresponding to the octahedral tilting in the orthorhombic structure have the largest amplitudes; however, amplitudes of the X_5^+ and R_5^+ modes related to the displacement of the A cations (X_5^+ A and R_5^+ A) and the amplitude of the X_5^+ mode related to the displacement of the oxygen atoms (X_5^+ O) are not negligible and indicate that $Fe^{3+}AlO_3$ substitution causes an even greater degree of distortion of both B and A sites than found in $MgSiO_3$ Brg (Figure 4). The X_5^+ O displacement and M_3^+ tilting appear to depend only on the extent of $M^{3+}M^{3+}O_3$ substitution as all samples, even those having a large Fe^{2+} content, plot on the same positive linear trends. The $Fe^{2+}SiO_3$ substitution, however, clearly has an effect on R_4^+ tilting and the A cation displacements (X_5^+ A and R_5^+ A), which are both smaller for Fe^{2+}-rich samples. This indicates that with increasing Fe^{2+} substitution, the Brg crystal structure becomes less distorted and the A cation sits more toward the center of the polyhedral site compared to $MgSiO_3$ Brg.

The oxygens and A-site cation displacements caused by the substitution of different cations determine the variations of bond distances, polyhedral distortions, and unit-cell parameters, which all ultimately control the compressibility behavior of these Brgs. By analyzing the structural changes occurring in the samples, the effects of several different substitution mechanisms can be resolved to some extent. Substitution of Al into the B-site causes an increase in the octahedral volume due to the larger size of this cation with respect to Si. As the oxygen displacements have to follow the symmetry rules, as described by the Irreps, the increase in the three different B-O bond distances, as Al is added, cannot be uniform and as shown in Figure 5a is quite anisotropic. The B-O1 bond distances involve the apical oxygens (O1) whose displacements (R_4^+ and X_5^+ O; Figure 1b) occur on the a–b plane away from the A cations and are, therefore, less restricted in their motion than the O2. As a result, the B-O1 bond distances increase more steeply, giving rise to an elongation of the

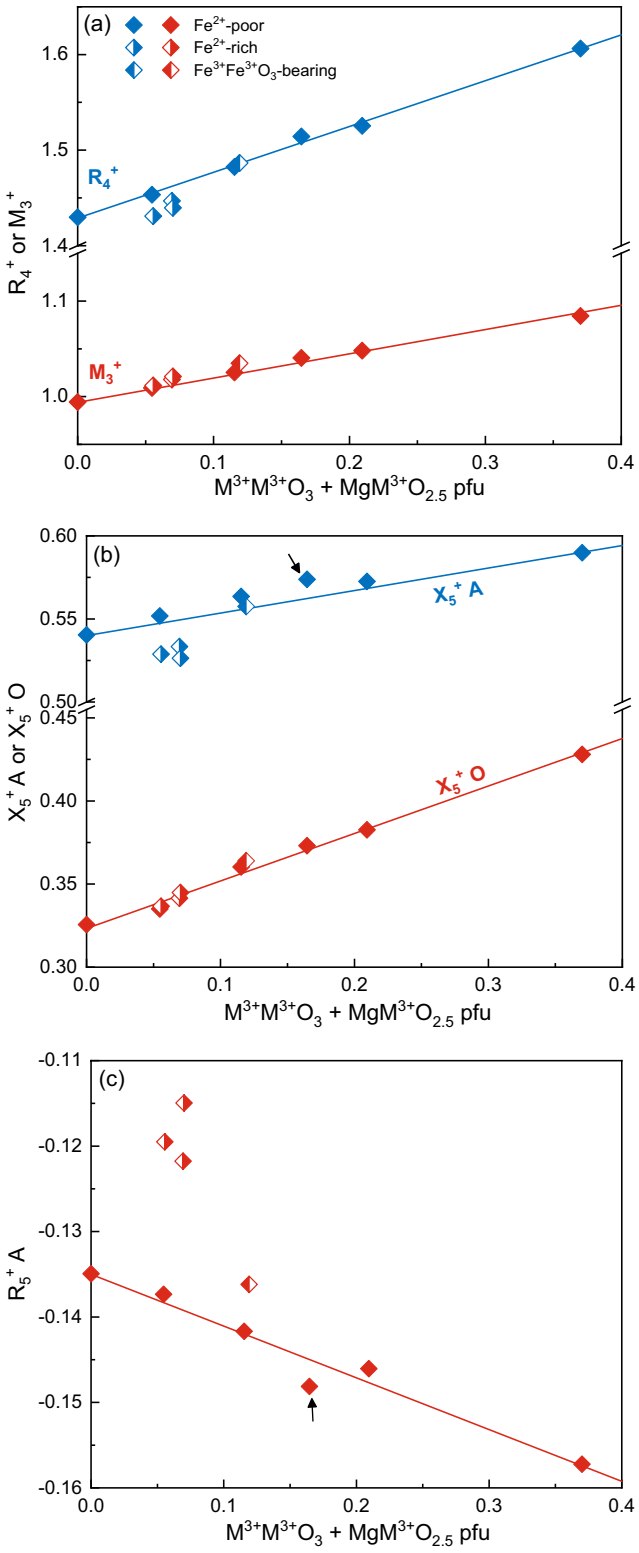

Figure 4. Variation of the amplitudes of the main distortion modes in the Brg structure as a function of the summation of charge-coupled and oxygen vacancy components. The Irreps R_4^+ and M_3^+ are related to the orthorhombic octahedral tilting, whereas the Irreps X_5^+ A, X_5^+ O and R_5^+ A represent the distortions of the octahedral and A site. Symbols are the same as in Figure 2a. Errors are within the symbol size. The small black arrows in panels (b) and (c) indicate sample S7241 containing 0.02 atoms pfu Al on the A site.

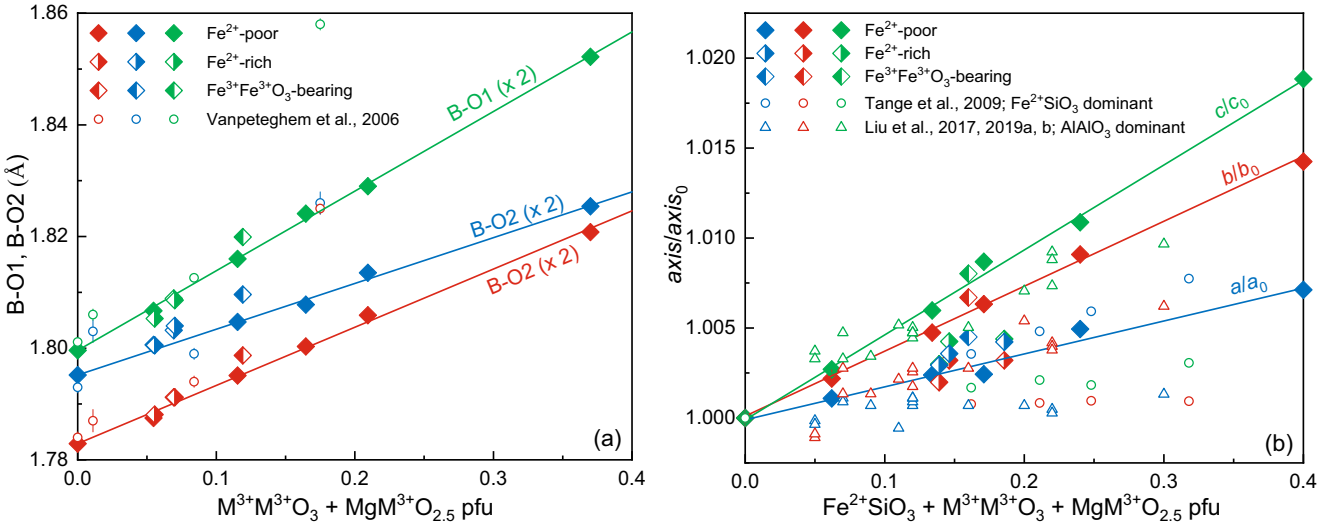

Figure 5. (a) Variation of individual B-O bond lengths of Brg as a function of the summation of charge-coupled and oxygen vacancy components. The number of equivalent octahedral bonds are reported in parentheses. Data from Vanpeteghem et al. (2006) indicated by open circles are also shown for comparison. (b) Variation of the unit cell parameters of Brg as a function of the sum of components other than $MgSiO_3$. Variation of Brg lattice parameters measured in this study are normalized to those of the $MgSiO_3$ endmember. Data from Tange et al. (2009) dominated by $Fe^{2+}SiO_3$ substitution and from Liu, Akaogi, and Katsura (2019); Liu, Ballaran, et al. (2019); Liu et al. (2017) dominated by $AlAlO_3$ substitution are also shown for comparison. Symbols are the same as in Figure 2a. Errors are within the symbol size when not indicated.

octahedron as the $Fe^{3+}AlO_3$ component is added (Figure 5a). Since the B-O1 bond distance lies mainly along the *c*-axis (Figure 1a), this unit-cell lattice parameter shows the greatest increase with $Fe^{3+}AlO_3$ substitution (Figure 5b). The variation of the other B–O2 bond distances (Figure 5a) results from displacements of the O2 atoms (R_4^+ and M_3^+, Figure 1b) that cause an increase in octahedral tilting, which is favored by the replacement of Mg by the smaller Fe^{3+} cation at the A-site, as described in the next paragraph. However, since each O2 atom forms a shorter B-O2 bond on one octahedron but is part of a longer B-O2 bond in the adjacent octahedron, a uniform elongation of both lengths is not possible; and as a consequence, the shortest distance increases more steeply than the longer in order to accommodate the larger Al cation. In this way, the two nonequivalent B-O2 bonds become more similar in length with increasing $Fe^{3+}AlO_3$, implying that the basal plane of the octahedron becomes more regular. The variation of the two nonequivalent B-O2 distances also determines in part the variation of the *a* and *b* unit-cell parameters (Figure 5b). The *b*-axis increases more than the *a*-axis upon $Fe^{3+}AlO_3$ substitution because the shorter B-O2 distance lies mainly in this direction. Sample S6838, which has Fe^{3+} > Al and is calculated to contain 0.04(1) atoms pfu of Fe^{3+} in the octahedral site (labeled in Figure 5a as $Fe^{3+}Fe^{3+}O_3$ bearing) clearly displays B-O bond distances that deviate from the general $Fe^{3+}AlO_3$ trend. B-O bond distances appear, therefore, to be very sensitive to Fe^{3+} substitution into the B site. Such a low concentration of Fe^{3+} at the B site would not be resolved in the refinement of the B-O bond distances, if there were significant disordering of Fe^{3+} and Al between the A and B sites in the investigated Brgs, further supporting the cation assignment strategy followed in this study.

Samples S6732, S6848, and S6805, which contain up to 0.12 atoms pfu of Fe^{2+}, have B-O distances that do not deviate significantly from the $Fe^{3+}AlO_3$ trend, implying that $Fe^{2+}SiO_3$ substitution has no apparent influence on the octahedral volume, V_B, in agreement with the results shown in Figure 3. The $Fe^{2+}SiO_3$ substitution affects only slightly the *c*- and *b*-axes, as shown by the samples analyzed by Tange et al. (2009) (Figure 5b) and as expected due to the substitution of Mg for just slightly larger Fe^{2+} at the A site. However, it does have a small effect on the *a*-axis, with samples analyzed by Tange et al. (2009) following a similar trend as that defined by the samples investigated in this study (Figure 5b). This may be explained by the displacement of the slightly larger Fe^{2+} more toward the center of the A site (Figures 4b and 4c). Note, however, that these changes are small compared to the changes occurring along the other two axes due to the incorporation of Al into the octahedron; and therefore, result in a much smaller increase in molar volume (Figure 2a) along the $MgSiO_3$-$Fe^{2+}SiO_3$ join. The samples analyzed by Vanpeteghem et al. (2006) are in

broad agreement with our results, except the sample with the highest $Fe^{3+}AlO_3$ content which also contains 0.03 atoms pfu of Ti in the octahedral site and, therefore, has much longer B-O bond distances (Figure 5a).

Substitution of Fe^{3+} into the A site causes the four shorter individual A-O bond distances (Figure 6a) to decrease and the other longer distances (Figures 6b and 6c) to increase. These changes are due both to the displacement of the Fe^{3+} at the A-site toward one side of the A polyhedron, as clearly seen in the increase of the X^{5+} A and R^{5+} A modes (Figures 1b, 4b and 4c) and due to the tilting of the octahedra (R_4^+ and M_3^+) in order to better coordinate the smaller A cations. As a consequence, the distortion of the A site increases. We can expect that Al substitution into the A site, through an $AlAlO_3$ component for example, will result in an even larger off-center displacement than Fe^{3+} given its smaller radius, which will further lead to a distortion of the A site and a larger increase in the octahedral tilting. This is supported by the deviation of sample S7241, which is the only sample with some Al on the A site and also plots below the R_5^+ A curve in Figure 4c and above the curve for X_5^+ A in Figure 4b (indicated by black arrows). This can explain the smaller unit-cell parameters of the $AlAlO_3$ samples (Figure 5b) in spite of them having octahedral volumes similar to the $Fe^{3+}AlO_3$ samples (Figure 3).

On the other hand, substitution of Fe^{2+} at the A site decreases the A-site distortion as well as the octahedral tilting. In fact, for the three Brg samples (S6732, S6848, and S6805) containing a larger amount of Fe^{2+}, the X_5^+ A and R_5^+ A modes are even smaller than those of the endmember $MgSiO_3$ (Figures 4b and 4c) that is, the cations are closer to the ideal cubic position. As a consequence, these three samples plot off some of the A-O distances trends (Figure 6). Moreover, the slightly larger Fe^{2+} cations require a smaller octahedral tilting (R_4^+ in Figures 1b and 4a) for their coordination. The individual A-O bond lengths of Brg from Vanpeteghem et al. (2006) also agree with our experiments, with the small deviations ascribable to the presence of other elements, as mentioned previously (Figure 6).

4. Discussion

4.1. Compressibility and Distortion of Bridgmanite With Pressure

Using the structural information obtained in this study, it is possible to rationalize how changes in tilting and distortion that occur upon certain substitutions are likely to influence the Brg bulk modulus (K). This can be used to evaluate previous experimental and *ab initio* determinations of these effects for different Brg substitutions, which are often in poor agreement. While the room pressure and temperature isothermal bulk modulus of endmember $MgSiO_3$ Brg is quite accurately determined to be 251 ± 2 GPa through compression experiments on $MgSiO_3$ Brg single-crystal (Boffa Ballaran et al., 2012), the effects on the Brg EoS of the substitution of other components are still quite poorly constrained. There are discrepancies, for example, as to whether the incorporation of Al into Brg would make it more or less compressible (Andrault et al., 2001; Daniel et al., 2001, 2004; Kubo et al., 2000; Walter et al., 2004, 2006; Yagi et al., 2004; Zhang & Weidner, 1999).

The compressibility of Brg will depend on the strength of the individual cation-oxygen bonds and, therefore, on the octahedral (β_B) and A-site (β_A) compressibilities. The bulk moduli of different Brg endmembers relative to the $MgSiO_3$ endmember can be rationalized in terms of changes in tilting and distortion occurring in the Brg structure whilst accommodating cation substitution. It has been shown that the relative compressibility β_B/β_A can be directly deduced from the basic bond-valence parameters (Brown & Altermatt, 1985) and bond lengths measured at room pressure (Angel et al., 2005; Zhao et al., 2004), according to the equation:

$$\frac{\beta_B}{\beta_A} = \frac{M_A}{M_B}, \tag{1}$$

where M_A and M_B represent the site bond-valence parameters defined as $M_i = \sum_{j=1}^{N_i}\left(R_{ij}/B\right)\exp\left(\left(R_0 - R_{ij}\right)/B\right)$ with R_0 the bond-valence parameter depending only upon the particular cation-anion pair; B a universal constant equal to 0.37 Å (Brese & O'Keeffe, 1991; Brown & Altermatt, 1985); R_{ij} and N_i the average bond length and coordination number of the cation site at ambient conditions, respectively. Since the Brgs investigated in this study do not have an endmember composition, we have used instead of an average, the individual bond lengths, and we have calculated R_0 as a linear combination of the bond-valence parameters for the Brg A and B sites. The resulting M_A/M_B ratios (Figure 7) are all

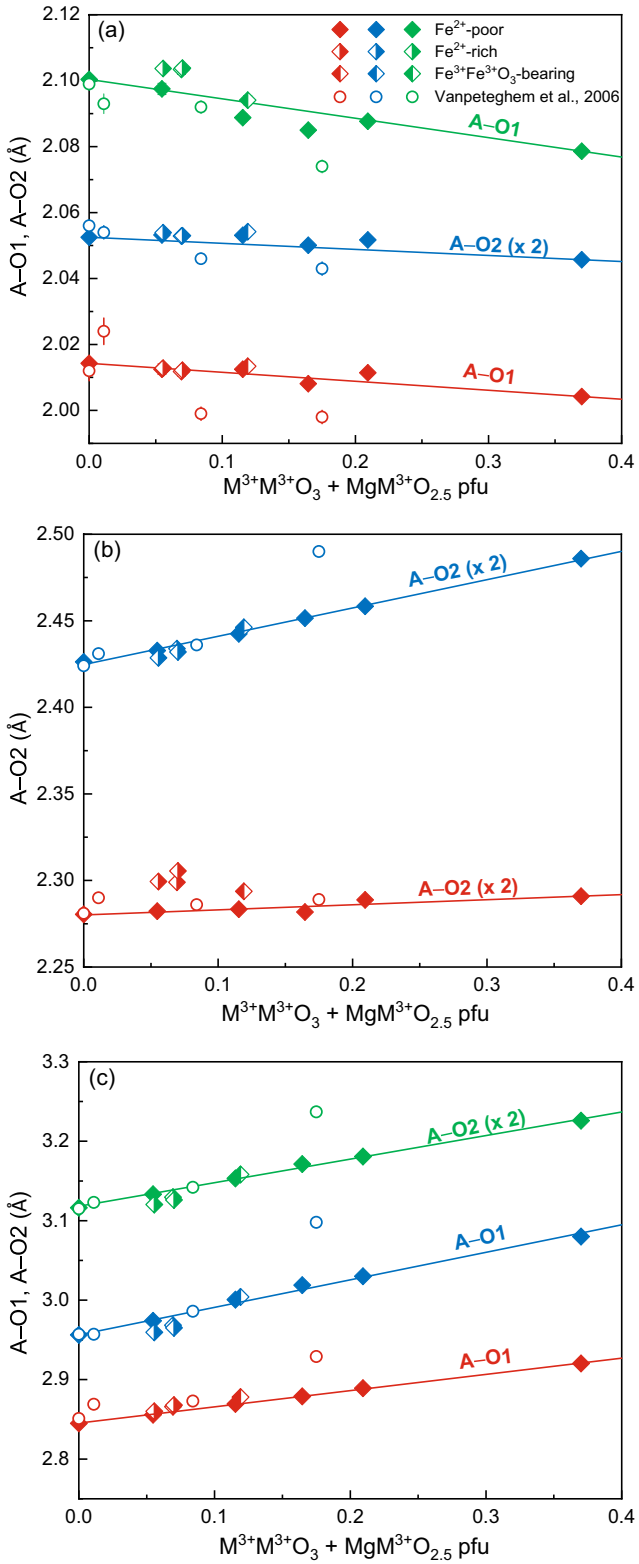

Figure 6. Variation of individual A-O bond distances as a function of the summation of charge-coupled and oxygen vacancy components. The number of equivalent A-O bonds are reported in parentheses. (a) Shortest A-O bonds; (b) Intermediate A-O bonds; and (c) Longest A-O bonds. Symbols are the same as in Figure 2a. The errors are within the symbol sizes.

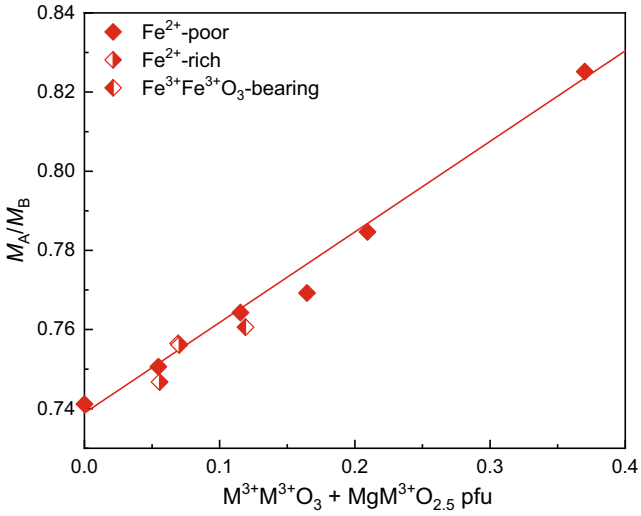

Figure 7. The relative compressibility of the B site over A site ($M_A/M_B = \beta_B/\beta_A$) versus the sum of charge-coupled and oxygen vacancy substitution in Brg. Symbols are the same as in Figure 2a.

<1 implying that the A site is more compressible than the octahedral site (Angel et al., 2005) and that, therefore, the compression of the octahedral framework will be mainly responsible for the bulk compressibility of Brg. The M_A/M_B ratio also increases with increasing $Fe^{3+}AlO_3$ substitution, implying an increase in octahedral compressibility and/or a decrease in the A-site compressibility with respect to $MgSiO_3$ Brg. The increase in octahedral compressibility is due to Al substituting for Si at the B site and it is likely the major cause of the previously reported decrease in the bulk modulus of Brg by $Fe^{3+}AlO_3$ substitution (Boffa Ballaran et al., 2012; Nishio-Hamane et al., 2008). Since the same type of octahedral substitution also occurs in $AlAlO_3$, this component should also have a smaller bulk modulus than $MgSiO_3$. Substitution of Fe^{3+} at the octahedral site should further increase its compressibility resulting in an even more compressible $Fe^{3+}Fe^{3+}O_3$ component. Due to the presence of both Al at the octahedral site and oxygen vacancies, we would expect $MgAlO_{2.5}$ Brg to be softer than $AlAlO_3$. Following the same argument, we would expect $MgFe^{3+}O_{2.5}$ Brg to be the softest of all components.

Based on this information, we attempt to make estimates for the room pressure and temperature bulk modulus of different Brg endmembers by selecting studies from the literature and using the relation,

$$K = \frac{V}{\sum_{i=1}^{N} \frac{x_i V_i}{K_i}}, \quad (2)$$

where K and V are the bulk modulus and volume, respectively, of a Brg with mixed composition, x_i is the mole fraction of the component i in the Brg of mixed composition and K_i and V_i are the bulk modulus and molar volume of the pure i component. The bulk modulus of pure $MgSiO_3$ Brg as well as the experimental data used to constrain the bulk modulus of $Fe^{3+}AlO_3$ are taken from the single-crystal compression study of Boffa Ballaran et al. (2012). Sample S4253 in this previous study contains a high proportion of the $Fe^{3+}AlO_3$ component (0.37 pfu) and thus should provide good constraints on the endmember value of K_i, which is determined to be 224 GPa. There are significant discrepancies in the literature as to the extent to which Al on its own influences Brg compressibility. Some studies show a substantial decrease of K_i (8%–12%) even with a small amount of Al (5–7.7 mol.%) (Daniel et al., 2001; Kubo et al., 2000; Zhang & Weidner, 1999) while others predict a smaller effect, that is, a ~2.5% decrease with 10 mol.% Al (Daniel et al., 2004; Walter et al., 2004). This discrepancy may well result from differing proportions of $AlAlO_3$ CC and $MgAlO_{2.5}$ OV components in the investigated samples, with higher compressibilities related to the latter (Daniel et al., 2004; Walter et al., 2004). One of the only studies to specifically address this is the *ab initio* study of Brodholt (2000). By normalizing the values in this previous study to account for the fact that the generalized gradient approximation (GGA) tends to underestimate K_i by about 7%–8% (Brodholt, 2000), a value for the $AlAlO_3$ endmember of 200 GPa is obtained, which is in good agreement with the trend reported by Walter et al. (2004). The different cation substitutions at the A site should obviously account for the different compressibilities of the $Fe^{3+}AlO_3$ and $AlAlO_3$ components. Although Fe^{3+} is larger than Al and would, therefore, be expected to be more compressible, the calculations described above imply that $Fe^{3+}AlO_3$ is slightly stiffer than $AlAlO_3$. This is likely due to the slightly greater off-center displacement of Al with respect to Fe^{3+} (Figures 4b and 4c), which leads to an increase in the longer A-O bonds. Interestingly, as described in Section 3.3, $Fe^{2+}SiO_3$ substitution causes the opposite effect, making the A cation more centered in the polyhedron, which might be coupled to a small increase in the bulk modulus upon Fe^{2+} substitution, as proposed in some studies (e.g., Boffa Ballaran et al., 2012; Dorfman et al., 2013; Kiefer et al., 2002; Lundin et al., 2008; Mao et al., 2011).

Making the same GGA correction to the data of Brodholt (2000) gives a K_i for the $MgAlO_{2.5}$ endmember of 163 GPa. This increase in the compressibility (35%) is slightly larger than that (25%) proposed by Ross et al. (2002) based on a comparison between the $CaFeO_{2.5}$ brownmillerite structure and OV-free perovskites. These could both be overestimates, however, as they consider OVs to be fully ordered, which is most likely

Table 4
Volume Changes for Equilibria Involving Brg and Ferropericlase Components and Iron Metal at Various Pressure and Temperature Conditions

	0 GPa, RT	25 GPa, 1900 K		50 GPa, 2064 K	
(1) $2MgAlO_{2.5} = AlAlO_3 + 2MgO$	−4.96	−5.18	−3.67	−5.34	−3.22
(2) $2MgFeO_{2.5} = Fe^{3+}Fe^{3+}O_3 + 2MgO$	−3.27	−3.58	−2.77	−3.84	−2.67
(3) $AlAlO_3 + Fe^{3+}Fe^{3+}O_3 = 2Fe^{3+}AlO_3$	−1.21	−1.15	0.10	−1.07	0.65
(4) $3FeO + AlAlO_3 = 2Fe^{3+}AlO_3 + Fe$	−1.35	−0.13	−0.15	0.61	0.57
(5) $3FeO = Fe^{3+}Fe^{3+}O_3 + Fe$	−0.14	1.01	−0.24	1.68	−0.08
(6) $3Fe^{2+}SiO_3 = Fe^{3+}Fe^{3+}O_3 + Fe + 3SiO_2$	2.61	2.81	1.14	2.88	0.37
(7) $3Fe^{2+}SiO_3 + AlAlO_3 = 2FeAlO_3 + Fe + 3SiO_2$	1.40	1.67	1.24	1.81	1.02

Notes. All values are in cm^3/mole. The first column at each pressure and temperature condition is the result assuming Brg component equation of state (EoS) are identical to those of $MgSiO_3$ Brg, while the second column uses EoS terms given in Table S5. Details are described in the text and notes of Table S5.

not the case for Brg (Grüninger et al., 2019). K_i for the $Fe^{3+}Fe^{3+}O_3$ component can be determined using data for a $Mg_{0.915}Fe^{3+}_{0.085}Si_{0.915}Fe^{3+}_{0.085}O_3$ Brg reported by Catalli et al. (2010). The resulting value of 155 GPa is in excellent agreement with the value of 157 GPa obtained from the theoretical study of Shukla et al. (2016). As $Fe^{3+}Fe^{3+}O_3$ substitution will cause a large decrease in the bulk modulus of Brg, studies on the effect of $Fe^{2+}SiO_3$ substitution need to be very clear on the iron oxidation state of the samples. Values of K_i for different Brg endmembers are summarized in Table S5. Due to the lack of experimental and theoretical constraints, the bulk modulus of $MgFe^{3+}O_{2.5}$ is assumed to be identical to that of the $MgAlO_{2.5}$ component in the following discussion.

4.2. Variation of Different Bridgmanite Components With Pressure

The molar volumes and isothermal bulk moduli of different Brg endmembers determined in this study, together with other thermodynamic data tabulated in Table S5, can be used to calculate the volume changes (ΔV) associated with different equilibria involving the Brg components, Fp and iron metal at different pressures (Table 4). This allows the likely effect of pressure on the proportions of Brg components to be assessed. The values of ΔV are calculated at high-pressure and temperature using the modified Tait equation of state (TEOS) (Holland & Powell, 2011) and either using the EoS parameters for each Brg component given in Table S5 or assuming that all Brg component bulk moduli are identical to the bulk modulus of $MgSiO_3$ Brg. A comparison between the two ΔV estimates is used to provide some considerations of the likely uncertainties on ΔV.

Equilibria (1) and (2) (Table 4), which monitor respectively the preference for the formation of the OV components versus the CC equivalents, have relatively large negative values of ΔV at all conditions examined, regardless of the EoS parameters used. This implies that pressure will drive these equilibria to the right, favoring the CC substitution mechanism over the OV substitution at the top of the lower mantle, in good agreement with recent experimental studies (Liu et al., 2017; Walter et al., 2006). Equilibrium (3) (Table 4) examines the preference for Fe^{3+} and Al ordering with increasing pressure. The sign of the ΔV can be seen to vary depending on the EoS parameters used. The study of Catalli et al. (2010) implies a relatively high compressibility for $Fe^{3+}Fe^{3+}O_3$ Brg, leading to positive estimates for equilibrium (3), which would favor disordering of Fe^{3+} and Al onto both sites with increasing pressure. This agrees with several experimental and computational studies that suggest that Fe^{3+} enters the B-site of Fe and Al-bearing Brg at pressures above 50 GPa, likely due to the high-spin to low-spin transition of octahedrally coordinated Fe^{3+} with consequent reduction of its cation size (Catalli et al., 2011; Fujino et al., 2012; Hsu et al., 2012). Although other studies have, however, questioned these results (Glazyrin et al., 2014; Kupenko et al., 2015), some degree of Al/Fe^{3+} disorder seems plausible within the current uncertainties. Equilibrium (4) describes the disproportionation of Fe^{2+} to produce the $Fe^{3+}AlO_3$ Brg component and iron metal. While the equilibrium ΔV is predicted to be negative at 25 GPa, at 50 GPa it becomes positive, irrespective of the EoS parameters used, suggesting that the proportion of iron metal formed in the mantle decreases with increasing pressure. However, the

formation of iron metal can occur also due to the formation of the $Fe^{3+}Fe^{3+}O_3$ Brg component (equilibrium 5 in Table 4). In this case, the disproportionation of Fe^{2+} to form $Fe^{3+}Fe^{3+}O_3$ and iron metal is still favored at 50 GPa. Above 50 GPa, the high-spin to low-spin transition of Fe^{2+} in Fp may eventually drive equilibrium (5) to the left. This tendency for the amount of disproportionated metal to first increase and then decrease with pressure would mean that the fo_2 would also first decrease and then increase with pressure. As a result, the deep lower mantle maybe less reduced than the shallower region, although there is no reason to believe that the effect is sufficient for the fo_2 to be raised significantly above the IW buffer (Huang et al., 2021). Higher temperatures during magma ocean crystallization may have further suppressed the amount of metal formed through disproportionation due to the requirement for lower Fe^{3+} contents in Brg in equilibrium with iron metal at these conditions (Boujibar et al., 2016; Frost et al., 2004; Huang et al., 2021). As indicated above, metal production may have then been further suppressed at pressures above 50 GPa, although removal of metal by core forming liquids as they pass through the shallow lower mantle remains a viable mechanism for mantle oxidation.

A relatively sharp decrease in the $Fe^{3+}/\sum Fe$ ratio of Brg in the presence of iron metal was reported between 35 and 51 GPa in the laser heated DAC study of Shim et al. (2017). In this study, Brg coexisted with metallic iron but in some experiments a small amount of silica was detected. As the experiments did not contain Fp, the experiments of Shim et al. (2017) may be explained at these pressures by considering the volume changes of equilibria (6) and (7) (Table 4). Both equilibria show positive volume changes at 25 and 50 GPa, regardless of the bulk modulus assumptions made (Table 4), implying that the $Fe^{3+}/\sum Fe$ ratio in Brg should decrease with pressure as observed by Shim et al. (2017). However, such a decrease might not be expected for a pyrolitic mantle containing Fp, for which equilibria (4) and (5) (Table 4) are likely more applicable. Fe and Al-rich Brg in subducted oceanic crust would coexist with free silica in the lower mantle (Akaogi, 2007; Hirose et al., 2005). Since our calculation shows that pressure may not favor FeO charge disproportionation in silica saturated systems, when considering also the more oxidized nature and smaller proportion of Brg in oceanic crust compared with pyrolitic mantle, disproportionation to form iron metal might not be expected to occur in subducted oceanic crust.

5. Conclusions

The crystal chemistry of ten well-characterized Al and Fe-bearing Brg single-crystals with Fe and Al contents ranging from 0 to 0.40 atoms pfu were investigated by single-crystal X-ray diffraction. Structural refinements confirm the preference of Fe^{3+} and Al for the A and B sites, respectively. Charge-coupled substitution is dominant for trivalent cations (Fe^{3+} and Al^{3+}) and the oxygen vacancy component does not exceed 0.04 pfu for the investigated Brg crystals. Through the site assignment, a small amount of Fe^{3+} (0.04 atoms pfu) was found to enter the B site in one of the samples due to the concentration of Fe^{3+} exceeding Al. In one Al-rich sample ($Al > Fe^{3+}$) a small amount of Al is assigned to the A site. Based on the compositions and molar volumes of Brg, the molar volumes of important Brg endmember components were refined by linear regression, using also data from previous studies, and found to decease in the order $Fe^{3+}Fe^{3+}O_3 > MgFe^{3+}O_{2.5} > Fe^{3+}AlO_3 > MgAlO_{2.5} > AlAlO_3 > Fe^{2+}SiO_3 > MgSiO_3$.

$Fe^{3+}AlO_3$ substitution leads to increasing octahedral tilting to accommodate the smaller A cations. Moreover, the B-O bond distances increase anisotropically with the longest B-O1 bonds increasing the most and the longer B-O2 bond increasing the least, resulting in a more distorted octahedron but with a more regular basal plane. As the B-O1 bond lies along the *c*-axis, it increases more than the *b*- and *a*-axis upon $Fe^{3+}AlO_3$ substitution. The larger displacement of the A cation from the center position of the A polyhedron also causes the four shorter individual A-O bond distances to decrease and the other longer distances to increase. The Al-rich sample, which hosts some Al on the A site, shows a greater off-center A cation displacement, which probably contributes to the smaller molar volume increase for $AlAlO_3$ substitution and may explain higher compressibilities proposed for this endmember compared to $Fe^{3+}AlO_3$. In contrast, $Fe^{2+}SiO_3$ substitution decreases the R_4^+ octahedral tilting and A site displacement, giving rise to the least distorted Brg perovskite structure. Based on the strength of individual A-O and B-O bonds, the A site appears to be more compressible than the B site in Brg, therefore octahedral tilting and distortion are mainly responsible for the compressibility in Brg. Even a small component of B-site Fe^{3+}, implied in the site assignment when $Fe^{3+} > Al$, leads to a clear increase in B-O bond distances and consequently the molar volume. The fact that

this is so visible at low concentrations implies that Fe^{3+} and Al are highly ordered between the A and B sites, respectively, when Fe^{3+} = Al.

Guided by the expected structural influences of different substitutions, the bulk moduli of trivalent cation Brg endmember components were estimated using elasticity data from previous studies. The volume changes (ΔV) associated with different equilibria involving the Brg components, Fp and iron metal at different pressures and temperatures were then calculated using the modified Tait equation of state. The results indicate that $AlAlO_3$ and $Fe^{3+}Fe^{3+}O_3$ charge-coupled substitutions are more favorable than oxygen vacancy substitution with increasing pressure. Moreover, pressure may favor Fe^{3+} and Al disordering. The production of Fe metal by disproportionation of FeO with the formation of the $Fe^{3+}AlO_3$ Brg component is promoted at 25 GPa but is predicted to become less favorable by 50 GPa. However, if $Fe^{3+}Fe^{3+}O_3$ Brg is very compressible, as suggested by one experimental study, the disproportionation of Fe^{2+} to form $Fe^{3+}Fe^{3+}O_3$ and iron metal may still be favored at 50 GPa.

Conflict of Interest

The authors declare no conflicts of interest relevant to this study.

Data Availability Statement

All the data to produce the results are available on Zenodo (https://doi.org/10.5281/zenodo.5146796) and can be found in Tables 1–4 and the online supporting information.

Acknowledgments
The authors acknowledge H. Fischer for high-pressure cell assembly machining, R. Njul for sample preparation and D. Krauße and A. Potzel for assistance with EPMA analysis. The manuscript was greatly improved by the constructive comments of Michael J. Walter and an anonymous reviewer. This work was supported by DFG grant FR1555/11. The Titan G2 TEM and Scios FIB at BGI were financed by DFG grants No. INST 91/315-1 FUGG and INST 91/251-1 FUGG, respectively. Open access funding enabled and organized by Projekt DEAL.

References

Akaogi, M. (2007). Phase transitions of minerals in the transition zone and upper part of the lower mantle. In Ohtani, E. (Ed.), *Advances in high-pressure mineralogy* (pp. 1–13). Geological Society of America.

Allen, F., Kennard, O., Watson, D., Brammer, L., Orpen, A., & Taylor, R. (1992). *International tables for crystallography* (Vol. C). Kluwer Academic Publishers.

Andrault, D., Bolfan-Casanova, N., Bouhifd, M. A., Guignot, N., & Kawamoto, T. (2007). The role of Al-defects on the equation of state of Al-(Mg,Fe)SiO_3 perovskite. *Earth and Planetary Science Letters*, *263*, 167–179. https://doi.org/10.1016/j.epsl.2007.08.012

Andrault, D., Bolfan-Casanova, N., & Guignot, N. (2001). Equation of state of lower mantle (Al, Fe)-$MgSiO_3$ perovskite. *Earth and Planetary Science Letters*, *193*, 501–508. https://doi.org/10.1016/s0012-821x(01)00506-4

Andrault, D., Neuville, D. R., Flank, A.-M., & Wang, Y. (1998). Cation sites in Al-rich $MgSiO_3$ perovskites. *American Mineralogist*, *83*, 1045–1053. https://doi.org/10.2138/am-1998-9-1013

Angel, R. J., Downs, R. T., & Finger, L. W. (2000). High-temperature-high-pressure diffractometry. *Reviews in Mineralogy and Geochemistry*, *41*, 559–597. https://doi.org/10.1515/9781501508707-020

Angel, R. J., & Finger, L. W. (2011). SINGLE: A program to control single-crystal diffractometers. *Journal of Applied Crystallography*, *44*, 247–251. https://doi.org/10.1107/S0021889810042305

Angel, R. J., Zhao, J., & Ross, N. L. (2005). General rules for predicting phase transitions in perovskites due to octahedral tilting. *Physical Review Letters*, *95*, 025503. https://doi.org/10.1103/PhysRevLett.95.025503

Becerro, A., McCammon, C., Langenhorst, F., Seifert, F., & Angel, R. (1999). Oxygen vacancy ordering in $CaTiO_3$-$CaFeO_{2.5}$ perovskites: From isolated defects to infinite sheets. *Phase Transitions: A Multinational Journal*, *69*, 133–146. https://doi.org/10.1080/01411599908208014

Boffa Ballaran, T., Kurnosov, A., Glazyrin, K., Frost, D. J., Merlini, M., Hanfland, M., & Caracas, R. (2012). Effect of chemistry on the compressibility of silicate perovskite in the lower mantle. *Earth and Planetary Science Letters*, *333–334*, 181–190. https://doi.org/10.1016/j.epsl.2012.03.029

Boujibar, A., Bolfan-Casanova, N., Andrault, D., Bouhifd, M. A., & Trcera, N. (2016). Incorporation of Fe^{2+} and Fe^{3+} in bridgmanite during magma ocean crystallization. *American Mineralogist*, *101*, 1560–1570. https://doi.org/10.2138/am-2016-5561

Brese, N., & O'Keeffe, M. (1991). Bond-valence parameters for solids. *Acta Crystallographica Section B: Structural Science*, *47*, 192–197. https://doi.org/10.1107/S0108768190011041

Brodholt, J. P. (2000). Pressure-induced changes in the compression mechanism of aluminous perovskite in the Earth's mantle. *Nature*, *407*, 620–622. https://doi.org/10.1038/35036565

Brown, I., & Altermatt, D. (1985). Bond-valence parameters obtained from a systematic analysis of the inorganic crystal structure database. *Acta Crystallographica Section B: Structural Science*, *41*, 244–247. https://doi.org/10.1107/S0108768185002063

Campbell, B. J., Stokes, H. T., Tanner, D. E., & Hatch, D. M. (2006). ISODISPLACE: A web-based tool for exploring structural distortions. *Journal of Applied Crystallography*, *39*, 607–614. https://doi.org/10.1107/S0021889806014075

Catalli, K., Shim, S.-H., Dera, P., Prakapenka, V. B., Zhao, J., Sturhahn, W., et al. (2011). Effects of the Fe^{3+} spin transition on the properties of aluminous perovskite—New insights for lower-mantle seismic heterogeneities. *Earth and Planetary Science Letters*, *310*, 293–302. https://doi.org/10.1016/j.epsl.2011.08.018

Catalli, K., Shim, S.-H., Prakapenka, V. B., Zhao, J., Sturhahn, W., Chow, P., et al. (2010). Spin state of ferric iron in $MgSiO_3$ perovskite and its effect on elastic properties. *Earth and Planetary Science Letters*, *289*, 68–75. https://doi.org/10.1016/j.epsl.2009.10.029

Daniel, I., Bass, J. D., Fiquet, G., Cardon, H., Zhang, J., & Hanfland, M. (2004). Effect of aluminum on the compressibility of silicate perovskite. *Geophysical Research Letters*, *31*. https://doi.org/10.1029/2004GL020213

Daniel, I., Cardon, H., Fiquet, G., Guyot, F., & Mezouar, M. (2001). Equation of state of Al-bearing perovskite to lower mantle pressure conditions. *Geophysical Research Letters*, *28*, 3789–3792. https://doi.org/10.1029/2001gl013011

Dorfman, S. M., Meng, Y., Prakapenka, V. B., & Duffy, T. S. (2013). Effects of Fe-enrichment on the equation of state and stability of (Mg, Fe) SiO_3 perovskite. *Earth and Planetary Science Letters*, *361*, 249–257. https://doi.org/10.1016/j.epsl.2012.10.033

Farrugia, L. J. (1999). WinGX suite for small-molecule single-crystal crystallography. *Journal of Applied Crystallography*, *32*, 837–838. https://doi.org/10.1107/S0021889899006020

Fei, Y., Wang, Y., & Finger, L. W. (1996). Maximum solubility of FeO in (Mg,Fe)SiO_3-perovskite as a function of temperature at 26 GPa: Implication for FeO content in the lower mantle. *Journal of Geophysical Research*, *101*, 11525–11530. https://doi.org/10.1029/96jb00408

Frost, D. J. (2008). The upper mantle and transition zone. *Elements*, *4*, 171–176. https://doi.org/10.2113/gselements.4.3.171

Frost, D. J., & Langenhorst, F. (2002). The effect of Al_2O_3 on Fe-Mg partitioning between magnesiowüstite and magnesium silicate perovskite. *Earth and Planetary Science Letters*, *199*, 227–241. https://doi.org/10.1016/S0012-821X(02)00558-7

Frost, D. J., Liebske, C., Langenhorst, F., McCammon, C. A., Trønnes, R. G., & Rubie, D. C. (2004). Experimental evidence for the existence of iron-rich metal in the Earth's lower mantle. *Nature*, *428*, 409–412. https://doi.org/10.1038/nature02413

Fujino, K., Nishio-Hamane, D., Seto, Y., Sata, N., Nagai, T., Shinmei, T., et al. (2012). Spin transition of ferric iron in Al-bearing Mg-perovskite up to 200 GPa and its implication for the lower mantle. *Earth and Planetary Science Letters*, *317–318*, 407–412. https://doi.org/10.1016/j.epsl.2011.12.006

Glazer, A. (1972). The classification of tilted octahedra in perovskites. *Acta Crystallographica Section B: Structural Crystallography and Crystal Chemistry*, *28*, 3384–3392. https://doi.org/10.1107/S0567740872007976

Glazyrin, K., Boffa Ballaran, T., Frost, D. J., McCammon, C. A., Kantor, A., Merlini, M., et al. (2014). Magnesium silicate perovskite and effect of iron oxidation state on its bulk sound velocity at the conditions of the lower mantle. *Earth and Planetary Science Letters*, *393*, 182–186. https://doi.org/10.1016/j.epsl.2014.01.056

Grüninger, H., Liu, Z., Siegel, R., Boffa Ballaran, T., Katsura, T., Senker, J., & Frost, D. J. (2019). Oxygen vacancy ordering in aluminous bridgmanite in the Earth's lower mantle. *Geophysical Research Letters*, *46*, 8731–8740. https://doi.org/10.1029/2019GL083613

Hirose, K., Fei, Y., Ma, Y., & Mao, H.-K. (1999). The fate of subducted basaltic crust in the Earth's lower mantle. *Nature*, *397*, 53–56. https://doi.org/10.1038/16225

Hirose, K., Takafuji, N., Sata, N., & Ohishi, Y. (2005). Phase transition and density of subducted MORB crust in the lower mantle. *Earth and Planetary Science Letters*, *237*, 239–251. https://doi.org/10.1016/j.epsl.2005.06.035

Holland, T. J. B., & Powell, R. (2011). An improved and extended internally consistent thermodynamic dataset for phases of petrological interest, involving a new equation of state for solids. *Journal of Metamorphic Geology*, *29*, 333–383. https://doi.org/10.1111/j.1525-1314.2010.00923.x

Holzapfel, C., Rubie, D. C., Frost, D. J., & Langenhorst, F. (2005). Fe-Mg interdiffusion in (Mg,Fe)SiO_3 perovskite and lower mantle reequilibration. *Science*, *309*, 1707–1710. https://doi.org/10.1126/science.1111895

Horiuchi, H., Ito, E., & Weidner, D. J. (1987). Perovskite-type $MgSiO_3$: Single-crystal X-ray diffraction study. *American Mineralogist*, *72*, 357–360.

Howard, C. J., & Stokes, H. T. (1998). Group-theoretical analysis of octahedral tilting in perovskites. *Acta Crystallographica Section B: Structural Science*, *54*, 782–789. https://doi.org/10.1107/S0108768198004200

Howard, C. J., & Stokes, H. T. (2002). Group-theoretical analysis of octahedral tilting in perovskites. *Erratum. Acta Crystallographica Section B*, *58*, 565. https://doi.org/10.1107/S010876810200890X

Howard, C. J., & Stokes, H. T. (2005). Structures and phase transitions in perovskites—A group-theoretical approach. *Acta Crystallographica Section A: Foundations of Crystallography*, *61*, 93–111. https://doi.org/10.1107/S0108767304024493

Hsu, H., Yu, Y. G., & Wentzcovitch, R. M. (2012). Spin crossover of iron in aluminous $MgSiO_3$ perovskite and post-perovskite. *Earth and Planetary Science Letters*, *359*, 34–39. https://doi.org/10.1016/j.epsl.2012.09.029

Huang, R., Boffa Ballaran, T., McCammon, C. A., Miyajima, N., Dolejš, D., & Frost, D. J. (2021). The composition and redox state of bridgmanite in the lower mantle as a function of oxygen fugacity. *Geochimica et Cosmochimica Acta*, *303*, 110–136. https://doi.org/10.1016/j.gca.2021.02.036

Hummer, D. R., & Fei, Y. (2012). Synthesis and crystal chemistry of Fe^{3+}-bearing (Mg, Fe^{3+})(Si, Fe^{3+})O_3 perovskite. *American Mineralogist*, *97*, 1915–1921. https://doi.org/10.2138/am.2012.4144

Irifune, T. (1994). Absence of an aluminous phase in the upper part of the Earth's lower mantle. *Nature*, *370*, 131–133. https://doi.org/10.1038/370131a0

Irifune, T., Koizumi, T., & Ando, J.-i. (1996). An experimental study of the garnet-perovskite transformation in the system $MgSiO_3$-$Mg_3Al_2Si_3O_{12}$. *Physics of the Earth and Planetary Interiors*, *96*, 147–157. https://doi.org/10.1016/0031-9201(96)03147-0

Irifune, T., & Ringwood, A. E. (1987). Phase transformations in a harzburgite composition to 26 GPa: Implications for dynamical behaviour of the subducting slab. *Earth and Planetary Science Letters*, *86*, 365–376. https://doi.org/10.1016/0012-821X(87)90233-0

Irifune, T., Shinmei, T., McCammon, C. A., Miyajima, N., Rubie, D. C., & Frost, D. J. (2010). Iron partitioning and density changes of pyrolite in Earth's lower mantle. *Science*, *327*, 193–195. https://doi.org/10.1126/science.1181443

Ito, E., & Matsui, Y. (1978). Synthesis and crystal-chemical characterization of $MgSiO_3$ perovskite. *Earth and Planetary Science Letters*, *38*, 443–450. https://doi.org/10.1016/0012-821X(78)90119-X

Jephcoat, A., Hriljac, J., McCammon, C. A., O'Neill, H. S. C., Rubie, D. C., & Finger, L. (1999). High-resolution synchrotron X-ray powder diffraction and Rietveld structure refinement of two ($Mg_{0.95}$,$Fe_{0.05}$)SiO_3 perovskite samples synthesized under different oxygen fugacity conditions. *American Mineralogist*, *84*, 214–220. https://doi.org/10.2138/am-1999-0301

Kennedy, B. J., Howard, C. J., & Chakoumakos, B. C. (1999). Phase transitions in perovskite at elevated temperatures-a powder neutron diffraction study. *Journal of Physics: Condensed Matter*, *11*, 1479–1488. https://doi.org/10.1088/0953-8984/11/6/012

Kiefer, B., Stixrude, L., & Wentzcovitch, R. (2002). Elasticity of (Mg,Fe)SiO_3-perovskite at high pressures. *Geophysical Research Letters*, *29*, 1539. https://doi.org/10.1029/2002GL014683

King, H., & Finger, L. (1979). Diffracted beam crystal centering and its application to high-pressure crystallography. *Journal of Applied Crystallography*, *12*, 374–378. https://doi.org/10.1107/S0021889879012723

Kojitani, H., Katsura, T., & Akaogi, M. (2007). Aluminum substitution mechanisms in perovskite-type $MgSiO_3$: An investigation by Rietveld analysis. *Physics and Chemistry of Minerals*, *34*, 257–267. https://doi.org/10.1007/s00269-007-0144-z

Kubo, A., Ono, S., & Akaogi, M. (2000). Compressibility of $Mg_{0.9}Al_{0.2}Si_{0.9}O_3$ perovskite. *Proceedings of the Japan Academy, Series B*, *76*, 103–107. https://doi.org/10.2183/pjab.76.103

Kudoh, Y., Prewitt, C., Finger, L., Darovskikh, A., & Ito, E. (1990). Effect of iron on the crystal structure of (Mg, Fe)SiO_3 perovskite. *Geophysical Research Letters*, *17*, 1481–1484. https://doi.org/10.1029/GL017i010p01481

Kupenko, I., McCammon, C. A., Sinmyo, R., Cerantola, V., Potapkin, V., Chumakov, A., et al. (2015). Oxidation state of the lower mantle: In situ observations of the iron electronic configuration in bridgmanite at extreme conditions. *Earth and Planetary Science Letters*, *423*, 78–86. https://doi.org/10.1016/j.epsl.2015.04.027

Kurnosov, A., Marquardt, H., Frost, D. J., Boffa Ballaran, T., & Ziberna, L. (2017). Evidence for a Fe^{3+}-rich pyrolitic lower mantle from (Al, Fe)-bearing bridgmanite elasticity data. *Nature*, *543*, 543–546. https://doi.org/10.1038/nature21390

Lauterbach, S., McCammon, C. A., vanAken, P., Langenhorst, F., & Seifert, F. (2000). Mössbauer and ELNES spectroscopy of (Mg,Fe)(Si,Al)O_3 perovskite: A highly oxidised component of the lower mantle. *Contributions to Mineralogy and Petrology*, *138*, 17–26. https://doi.org/10.1007/PL00007658

Lin, J.-F., Speziale, S., Mao, Z., & Marquardt, H. (2013). Effects of the electronic spin transitions of iron in lower mantle minerals: Implications for deep mantle geophysics and geochemistry. *Reviews of Geophysics*, *51*, 244–275. https://doi.org/10.1002/rog.20010

Litasov, K., Ohtani, E., Langenhorst, F., Yurimoto, H., Kubo, T., & Kondo, T. (2003). Water solubility in Mg-perovskites and water storage capacity in the lower mantle. *Earth and Planetary Science Letters*, *211*, 189–203. https://doi.org/10.1016/s0012-821x(03)00200-0

Liu, J., Dorfman, S. M., Zhu, F., Li, J., Wang, Y., Zhang, D., et al. (2018). Valence and spin states of iron are invisible in Earth's lower mantle. *Nature Communications*, *9*, 1284. https://doi.org/10.1038/s41467-018-03671-5

Liu, Z., Akaogi, M., & Katsura, T. (2019). Increase of the oxygen vacancy component in bridgmanite with temperature. *Earth and Planetary Science Letters*, *505*, 141–151. https://doi.org/10.1016/j.epsl.2018.10.014

Liu, Z., Boffa Ballaran, T., Huang, R., Frost, D. J., & Katsura, T. (2019). Strong correlation of oxygen vacancies in bridgmanite with Mg/Si ratio. *Earth and Planetary Science Letters*, *523*, 115697. https://doi.org/10.1016/j.epsl.2019.06.037

Liu, Z., Ishii, T., & Katsura, T. (2017). Rapid decrease of $MgAlO_{2.5}$ component in bridgmanite with pressure. *Geochemical Perspectives Letters*, *5*, 12–18. https://doi.org/10.7185/geochemlet.1739

Liu, Z., McCammon, C., Wang, B., Dubrovinsky, L., Ishii, T., Bondar, D., et al. (2020). Stability and solubility of the $FeAlO_3$ component in bridgmanite at uppermost lower mantle conditions. *Journal of Geophysical Research: Solid Earth*, *125*, e2019JB018447. https://doi.org/10.1029/2019JB018447

Lundin, S., Catalli, K., Santillán, J., Shim, S. H., Prakapenka, V. B., Kunz, M., & Meng, Y. (2008). Effect of Fe on the equation of state of mantle silicate perovskite over 1 Mbar. *Physics of the Earth and Planetary Interiors*, *168*, 97–102. https://doi.org/10.1016/j.pepi.2008.05.002

Mao, H.-K., Hemley, R. J., Fei, Y., Shu, J. F., Chen, L. C., Jephcoat, A. P., et al. (1991). Effect of pressure, temperature, and composition on lattice parameters and density of (Fe,Mg)SiO_3-perovskites to 30 GPa. *Journal of Geophysical Research*, *96*, 8069–8079. https://doi.org/10.1029/91jb00176

Mao, Z., Lin, J.-F., Scott, H., Watson, H., Prakapenka, V., Xiao, Y., et al. (2011). Iron-rich perovskite in the Earth's lower mantle. *Earth and Planetary Science Letters*, *309*, 179–184. https://doi.org/10.1016/j.epsl.2011.06.030

Mao, Z., Wang, F., Lin, J.-F., Fu, S., Yang, J., Wu, X., et al. (2017). Equation of state and hyperfine parameters of high-spin bridgmanite in the Earth's lower mantle by synchrotron X-ray diffraction and Mössbauer spectroscopy. *American Mineralogist*, *102*, 357–368. https://doi.org/10.2138/am-2017-5770

McCammon, C. A. (1997). Perovskite as a possible sink for ferric iron in the lower mantle. *Nature*, *387*, 694–696. https://doi.org/10.1038/42685

McCammon, C. A. (1998). The crystal chemistry of ferric iron in $Fe_{0.05}Mg_{0.95}SiO_3$ perovskite as determined by Mössbauer spectroscopy in the temperature range 80–293 K. *Physics and Chemistry of Minerals*, *25*, 292–300. https://doi.org/10.1007/s002690050117

McCammon, C. A., Glazyrin, K., Kantor, A., Kantor, I., Kupenko, I., Narygina, O., et al. (2013). Iron spin state in silicate perovskite at conditions of the Earth's deep interior. *High Pressure Research*, *33*, 663–672. https://doi.org/10.1080/08957959.2013.805217

McCammon, C. A., Rubie, D., Ross, C., Seifert, F., & O'Neill, H. S. C. (1992). Mössbauer spectra of $^{57}Fe_{0.05}Mg_{0.95}SiO_3$ perovskite at 80 and 298 K. *American Mineralogist*, *77*, 894–897.

Miller, S. C., & Love, W. F. (1967). *Tables of irreducible representations of space groups and co-representations of magnetic space groups*. Pruett Press.

Mitchell, R. H. (2002). *Perovskites: Modern and ancient*. Almaz Press.

Nakajima, Y., Frost, D. J., & Rubie, D. C. (2012). Ferrous iron partitioning between magnesium silicate perovskite and ferropericlase and the composition of perovskite in the Earth's lower mantle. *Journal of Geophysical Research*, *117*, B08201. https://doi.org/10.1029/2012JB009151

Navrotsky, A. (1999). A lesson from ceramics. *Science*, *284*, 1788–1789. https://doi.org/10.1126/science.284.5421.1788

Navrotsky, A., Schoenitz, M., Kojitani, H., Xu, H., Zhang, J., Weidner, D. J., & Jeanloz, R. (2003). Aluminium in magnesium silicate perovskite: Formation, structure, and energetics of magnesium-rich defect solid solutions. *Journal of Geophysical Research*, *108*, 2330. https://doi.org/10.1029/2002jb002055

Nishio-Hamane, D., Nagai, T., Fujino, K., Seto, Y., & Takafuji, N. (2005). Fe^{3+} and Al solubilities in $MgSiO_3$ perovskite: Implication of the $Fe^{3+}AlO_3$ substitution in $MgSiO_3$ perovskite at the lower mantle condition. *Geophysical Research Letters*, *32*, L16306. https://doi.org/10.1029/2005GL023529

Nishio-Hamane, D., Seto, Y., Fujino, K., & Nagai, T. (2008). Effect of $FeAlO_3$ incorporation into $MgSiO_3$ on the bulk modulus of perovskite. *Physics of the Earth and Planetary Interiors*, *166*, 219–225. https://doi.org/10.1016/j.pepi.2008.01.002

Ohta, K., Onoda, S., Hirose, K., Sinmyo, R., Shimizu, K., Sata, N., et al. (2008). The electrical conductivity of post-perovskite in Earth's D'' layer. *Science*, *320*, 89–91. https://doi.org/10.1126/science.1155148

Ono, S., Kikegawa, T., & Iizuka, T. (2004). The equation of state of orthorhombic perovskite in a peridotitic mantle composition to 80 GPa: Implications for chemical composition of the lower mantle. *Physics of the Earth and Planetary Interiors*, *145*, 9–17. https://doi.org/10.1016/j.pepi.2004.01.005

Parise, J., Wang, Y., Yeganeh-Haeri, A., Cox, D., & Fei, Y. (1990). Crystal structure and thermal expansion of (Mg,Fe)SiO_3 perovskite. *Geophysical Research Letters*, *17*, 2089–2092. https://doi.org/10.1029/GL017i012p02089

Perez-Mato, J. M., Orobengoa, D., & Aroyo, M. I. (2010). Mode crystallography of distorted structures. *Acta Crystallographica Section A*, *66*, 558–590. https://doi.org/10.1107/S0108767310016247

Prescher, C., McCammon, C. A., & Dubrovinsky, L. (2012). MossA: A program for analyzing energy-domain Mössbauer spectra from conventional and synchrotron sources. *Journal of Applied Crystallography*, *45*, 329–331. https://doi.org/10.1107/s0021889812004979

Ross, N. L., Angel, R., & Seifert, F. (2002). Compressibility of brownmillerite ($Ca_2Fe_2O_5$): Effect of vacancies on the elastic properties of perovskites. *Physics of the Earth and Planetary Interiors*, *129*, 145–151. https://doi.org/10.1016/S0031-9201(01)00269-2

Saikia, A., Boffa Ballaran, T., & Frost, D. J. (2009). The effect of Fe and Al substitution on the compressibility of $MgSiO_3$-perovskite determined through single-crystal X-ray diffraction. *Physics of the Earth and Planetary Interiors*, *173*, 153–161. https://doi.org/10.1016/j.pepi.2008.11.006

Shannon, R. D. (1976). Revised effective ionic radii and systematic studies of interatomic distances in halides and chalcogenides. *Acta Crystallographica - Section A: Crystal Physics, Diffraction, Theoretical and General Crystallography*, *32*, 751–767. https://doi.org/10.1107/S0567739476001551

Sheldrick, G. M. (2008). A short history of SHELX. *Acta Crystallographica Section A: Foundations of Crystallography*, *64*, 112–122. https://doi.org/10.1107/S0108767307043930

Shim, S.-H., Grocholski, B., Ye, Y., Alp, E. E., Xu, S., Morgan, D., et al. (2017). Stability of ferrous-iron-rich bridgmanite under reducing midmantle conditions. *Proceedings of the National Academy of Sciences*, *114*, 6468–6473. https://doi.org/10.1073/pnas.1614036114

Shukla, G., Cococcioni, M., & Wentzcovitch, R. M. (2016). Thermoelasticity of Fe^{3+}- and Al-bearing bridgmanite: Effects of iron spin crossover. *Geophysical Research Letters*, *43*, 5661–5670. https://doi.org/10.1002/2016gl069332

Sinmyo, R., Bykova, E., McCammon, C., Kupenko, I., Potapkin, V., & Dubrovinsky, L. (2014). Crystal chemistry of Fe^{3+}-bearing (Mg, Fe)SiO_3 perovskite: A single-crystal X-ray diffraction study. *Physics and Chemistry of Minerals*, *41*, 409–417. https://doi.org/10.1007/s00269-013-0639-8

Sinmyo, R., Hirose, K., Muto, S., Ohishi, Y., & Yasuhara, A. (2011). The valence state and partitioning of iron in the Earth's lowermost mantle. *Journal of Geophysical Research*, *116*, B07205. https://doi.org/10.1029/2010jb008179

Stebbins, J. F., Kojitani, H., Akaogi, M., & Navrotsky, A. (2003). Aluminum substitution in $MgSiO_3$ perovskite: Investigation of multiple mechanisms by ^{27}Al NMR. *American Mineralogist*, *88*, 1161–1164. https://doi.org/10.2138/am-2003-0724

Tange, Y., Takahashi, E., Nishihara, Y., Funakoshi, K.-i., & Sata, N. (2009). Phase relations in the system MgO-FeO-SiO_2 to 50 GPa and 2000°C: An application of experimental techniques using multianvil apparatus with sintered diamond anvils. *Journal of Geophysical Research*, *114*, B02214. https://doi.org/10.1029/2008jb005891

Thomas, N. W. (1989). Crystal structure–physical property relationships in perovskites. *Acta Crystallographica Section B: Structural Science*, *45*, 337–344. https://doi.org/10.1107/S0108768189003721

van Aken, P., & Liebscher, B. (2002). Quantification of ferrous/ferric ratios in minerals: New evaluation schemes of Fe $L_{2,3}$ electron energy-loss near-edge spectra. *Physics and Chemistry of Minerals*, *29*, 188–200. https://doi.org/10.1007/s00269-001-0222-6

van Aken, P., Liebscher, B., & Styrsa, V. (1998). Quantitative determination of iron oxidation states in minerals using Fe $L_{2,3}$-edge electron energy-loss near-edge structure spectroscopy. *Physics and Chemistry of Minerals*, *25*, 323–327. https://doi.org/10.1007/s002690050122

Vanpeteghem, C. B., Angel, R. J., Ross, N. L., Jacobsen, S. D., Dobson, D. P., Litasov, K. D., & Ohtani, E. (2006). Al, Fe substitution in the $MgSiO_3$ perovskite structure: A single-crystal X-ray diffraction study. *Physics of the Earth and Planetary Interiors*, *155*, 96–103. https://doi.org/10.1016/j.pepi.2005.10.003

Walter, M. J., Kubo, A., Yoshino, T., Brodholt, J., Koga, K. T., & Ohishi, Y. (2004). Phase relations and equation-of-state of aluminous Mg-silicate perovskite and implications for Earth's lower mantle. *Earth and Planetary Science Letters*, *222*, 501–516. https://doi.org/10.1016/j.epsl.2004.03.014

Walter, M. J., Trønnes, R. G., Armstrong, L. S., Lord, O. T., Caldwell, W. A., & Clark, S. M. (2006). Subsolidus phase relations and perovskite compressibility in the system MgO-$AlO_{1.5}$-SiO_2 with implications for Earth's lower mantle. *Earth and Planetary Science Letters*, *248*, 77–89. https://doi.org/10.1016/j.epsl.2006.05.017

Wang, Y., Weidner, D. J., Liebermann, R. C., & Zhao, Y. (1994). P-V-T equation of state of (Mg,Fe)SiO_3 perovskite: Constraints on composition of the lower mantle. *Physics of the Earth and Planetary Interiors*, *83*, 13–40. https://doi.org/10.1016/0031-9201(94)90109-0

Wolf, A. S., Jackson, J. M., Dera, P., & Prakapenka, V. B. (2015). The thermal equation of state of (Mg,Fe)SiO_3 bridgmanite (perovskite) and implications for lower mantle structures. *Journal of Geophysical Research: Solid Earth*, *120*, 7460–7489. https://doi.org/10.1002/2015JB012108

Wood, B., & Rubie, D. (1996). The effect of alumina on phase transformations at the 660-kilometer discontinuity from Fe-Mg partitioning experiments. *Science*, *273*, 1522–1524. https://doi.org/10.1126/science.273.5281.1522

Wood, B. J. (2000). Phase transformations and partitioning relations in peridotite under lower mantle conditions. *Earth and Planetary Science Letters*, *174*, 341–354. https://doi.org/10.1016/S0012-821X(99)00273-3

Xu, Y., McCammon, C. A., & Poe, B. T. (1998). The effect of alumina on the electrical conductivity of silicate perovskite. *Science*, *282*, 922–924. https://doi.org/10.1126/science.282.5390.922

Yagi, T., Mao, H.-K., & Bell, P. M. (1978). Structure and crystal chemistry of perovskite-type $MgSiO_3$. *Physics and Chemistry of Minerals*, *3*, 97–110. https://doi.org/10.1007/BF00308114

Yagi, T., Okabe, K., Nishiyama, N., Kubo, A., & Kikegawa, T. (2004). Complicated effects of aluminum on the compressibility of silicate perovskite. *Physics of the Earth and Planetary Interiors*, *143–144*, 81–91. https://doi.org/10.1016/j.pepi.2003.07.020

Zhang, J., & Weidner, D. J. (1999). Thermal equation of state of aluminum-enriched silicate perovskite. *Science*, *284*, 782–784. https://doi.org/10.1126/science.284.5415.782

Zhao, J., Ross, N., & Angel, R. (2004). New view of the high-pressure behaviour of $GdFeO_3$-type perovskites. *Acta Crystallographica Section B: Structural Science*, *60*, 263–271. https://doi.org/10.1107/S0108768104004276

Zhao, Y., Weidner, D. J., Parise, J. B., & Cox, D. E. (1993a). Critical phenomena and phase transition of perovskite—Data for $NaMgF_3$ perovskite. Part II. *Physics of the Earth and Planetary Interiors*, *76*, 17–16. https://doi.org/10.1016/0031-9201(93)90051-A

Zhao, Y., Weidner, D. J., Parise, J. B., & Cox, D. E. (1993b). Thermal expansion and structural distortion of perovskite—Data for $NaMgF_3$ perovskite. Part I. *Physics of the Earth and Planetary Interiors*, *76*, 1–34. https://doi.org/10.1016/0031-9201(93)90052-B

Reference From the Supporting Information

Campbell, A. J., Danielson, L., Righter, K., Seagle, C. T., Wang, Y., & Prakapenka, V. B. (2009). High pressure effects on the iron-iron oxide and nickel-nickel oxide oxygen fugacity buffers. *Earth and Planetary Science Letters*, *286*, 556–564. https://doi.org/10.1016/j.epsl.2009.07.022